PERGAMON

Available online at www.sciencedirect.com

SCIENCE DIRECT®

Computers & Fluids 33 (2004) 223–255

computers & fluids

www.elsevier.com/locate/compfluid

High order finite difference methods for unsteady incompressible flows in multi-connected domains

Jian-Guo Liu [a], Cheng Wang [b,*]

[a] *Department of Mathematics, Institute for Physical Science and Technology, University of Maryland, College Park, MD 20742, USA*

[b] *Department of Mathematics, Institute for Scientific Computing and Applied Mathematics, Indiana University, 831 East Third Street, Bloomington, IN 47405-5701, USA*

Received 23 July 2002; received in revised form 3 January 2003; accepted 4 February 2003

Abstract

Using the vorticity and stream function variables is an effective way to compute 2-D incompressible flow due to the facts that the incompressibility constraint for the velocity is automatically satisfied, the pressure variable is eliminated, and high order schemes can be efficiently implemented. However, a difficulty arises in a multi-connected computational domain in determining the constants for the stream function on the boundary of the ''holes''. This is an especially challenging task for the calculation of unsteady flows, since these constants vary with time to reflect the total fluxes of the flow in each sub-channel. In this paper, we propose an efficient method in a finite difference setting to solve this problem and present some numerical experiments, including an accuracy check of a Taylor vortex-type flow, flow past a non-symmetric square, and flow in a heat exchanger.

Keywords: Incompressible flow; Vorticity–stream function formulation; Multi-connected domain; Finite difference method

1. Introduction

The homogeneous, incompressible Navier–Stokes equations (NSE) in velocity–pressure formulation with no-slip boundary condition can be written as

* Corresponding author. Tel.: +1-812-855-9831.
E-mail addresses: jliu@math.umd.edu (J.-G. Liu), cwang@indiana.edu (C. Wang).

0045-7930/$ - see front matter
doi:10.1016/S0045-7930(03)00037-9

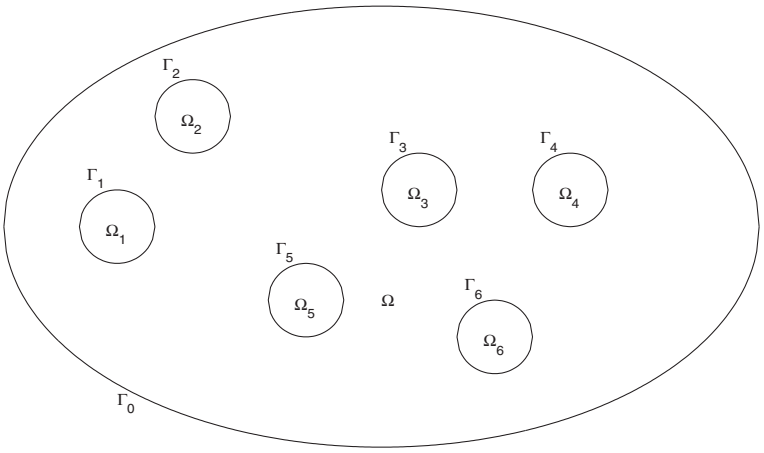

Fig. 1. An example of a 2-D multi-connected domain.

$$\begin{cases} \boldsymbol{u}_t + (\boldsymbol{u}\cdot\nabla)\boldsymbol{u} + \nabla p = \frac{1}{Re}\Delta\boldsymbol{u}, \quad \text{in } \Omega, \\ \nabla\cdot\boldsymbol{u} = 0, \quad \text{in } \Omega, \\ \boldsymbol{u} = 0, \quad \text{on } \partial\Omega, \end{cases} \tag{1.1}$$

where $\boldsymbol{u} = (u, v)$ is the velocity, p the pressure, and Re the Reynolds number. For simplicity, we denote $\nu = 1/Re$. In a multi-connected domain, $\partial\Omega$ is assumed to be composed of closed, non-intersecting segments Γ_i, $i = 1, \ldots, k$, enclosed by the closed curve Γ_0, i.e., $\partial\Omega = \Gamma_0 \cup \Gamma_1 \cup \Gamma_2 \cup \cdots \cup \Gamma_k$. The k regions with boundaries $\Gamma_1, \Gamma_2, \ldots, \Gamma_k$ correspond to the k "holes" of the domain Ω (see Fig. 1).

The no-penetration, no-slip boundary condition for the velocity is given by $\boldsymbol{u}|_{\Gamma_0} = 0, \boldsymbol{u}|_{\Gamma_1} = 0, \ldots, \boldsymbol{u}|_{\Gamma_k} = 0$.

There are many difficulties in the numerical simulation of incompressible flow in the primitive formulation, including enforcement of the incompressibility constraint $\nabla\cdot\boldsymbol{u} = 0$, lack of a dynamic equation and boundary condition for the pressure, and implementation of the no-penetration, no-slip boundary condition for the velocity $\boldsymbol{u}$. In the 2-D case, the first and second challenges can be overcome in the vorticity–stream function formulation

$$\begin{cases} \partial_t\omega + (\boldsymbol{u}\cdot\nabla)\omega = \nu\Delta\omega, \\ \Delta\psi = \omega, \\ u = -\partial_y\psi, \quad v = \partial_x\psi, \end{cases} \tag{1.2}$$

where the vorticity is defined as $\omega = \nabla\times\boldsymbol{u} = -\partial_y u + \partial_x v$.

The no-penetration boundary condition for $\boldsymbol{u}$ indicates that

$$\psi|_{\Gamma_i} = C_i, \quad \text{for } 0 \leqslant i \leqslant k, \tag{1.3}$$

where C_i are constants; while the no-slip boundary condition for $\boldsymbol{u}$ shows that

$$\frac{\partial\psi}{\partial\boldsymbol{n}} = 0, \quad \text{on each } \Gamma_i. \tag{1.4}$$

If a multi-connected computational domain is presented, an additional work to determine the constant C_i at the boundary section of each "hole" is needed. To proceed, we need to introduce the following equivalent formulation of the incompressible NSE in a multi-connected domain

$$\partial_t \omega + (\boldsymbol{u} \cdot \nabla)\omega = \nu \Delta \omega, \tag{1.5a}$$

$$\Delta \psi = \omega, \tag{1.5b}$$

$$\psi|_{\Gamma_i} = C_i, \quad \frac{\partial \psi}{\partial \boldsymbol{n}} = 0 \qquad \text{on each } \Gamma_i, \tag{1.5c}$$

$$\int_{\Gamma_i} \frac{\partial \omega}{\partial \boldsymbol{n}} = 0, \quad \text{for } 0 \leqslant i \leqslant k, \tag{1.5d}$$

$$u = -\partial_y \psi, \quad v = \partial_x \psi. \tag{1.5e}$$

Since the stream function is uniquely determined up to a constant, the constant on the outer boundary Γ_0 can be automatically set as 0, i.e., $C_0 = 0$.

The derivation of the boundary condition $\int_{\Gamma_i} \partial\omega/\partial\boldsymbol{n} = 0$ in (1.5d) is given below: on each boundary Γ_i, multiplying the momentum equation in (1.1) by τ (the unit tangential vector along the boundary) leads to

$$\frac{\partial p}{\partial \tau} = -\nu \frac{\partial \omega}{\partial \boldsymbol{n}}, \quad \text{on } \Gamma_i, \tag{1.6}$$

since the velocity $\boldsymbol{u}$ vanishes on the boundary. Integrating (1.6) along the boundary Γ_i, keeping in mind that p is a single-valued function, we arrive at the boundary condition in (1.5d). Such a derivation can also be found in [10,11,20,30].

A computational method of incompressible flow based on the vorticity formulation, (1.2)–(1.4), is a vast subject, and there are many issues and difficulties involved, such as:

(1) Determination of the stream function constant values, $C_1, C_2, \ldots, C_k$, on the boundary sections, with the no-flow, no-slip boundary condition in a multi-connected domain;
(2) Enforcement of the vorticity boundary condition;
(3) Large Reynolds number unsteady flow calculation;
(4) Far-field boundary condition;
(5) Fast convergence to the steady state flow, etc.

We refer to [28] for a comprehensive review of the subject. In this paper, we mainly concentrate on the first, in conjunction with the second and third issues. However, we shall point out that the algorithm proposed in this paper has limited application to other circumstances. For example, the iterative procedure proposed in this article to obtain the stream function constant at each boundary section may not be a good choice for a coupled biharmonic system. Several other simpler and better iterative procedures are available in steady state computations developed in the earlier literature. A thorough discussion on these issues can be found in [2,4–6,9,13,15–18,22–26,28,29].

For an unsteady flow at a large Reynolds number, we can maintain a stable and efficient numerical method by the explicit treatment of the convection and diffusion terms. The second order finite difference, fourth order compact difference schemes and the finite element method have been successfully carried out in [7,8,19]. Some difficulties involved with the vorticity boundary condition can be circumvented in these approaches. The no-slip boundary condition is enforced through a local vorticity boundary formula, such as Thom's [31] or Wilkes' formula in the second order method, and Briley's formula [3] in the fourth order method. To avoid the cell-Reynolds number constraint, high order time discretization, such as the fourth order Runge–Kutta method, was suggested.

Both the second and fourth order finite difference schemes of system (1.5) are formulated in this article. The main focus is on the implementation of boundary condition (1.5d), which is crucial to the determination of the stream function constant on the boundary. To illustrate the idea more clearly, we describe the second order method in detail in Section 2. A similar, brief discussion of the fourth order method is left for Section 3. Some iterative formulae, either (2.7) or (2.21) for the second order method, or (3.7) for the fourth order method, will be derived. Such formulae can be very efficiently applied in the Poisson solver of the kinematic relation between ψ and ω. No coupling between the momentum equation and the Poisson solver is needed.

For conciseness of presentation, we use a domain with a single square "hole", like in Fig. 2 below, as the example in the discussion of numerical schemes. Its extension to a general region with an arbitrary number of "holes" is straightforward. One only need to apply the iterative formula at each boundary section Γ_i of the holes. See Remarks 2.4 and 3.2 for the details.

In Section 4, we present some numerical examples, including an accuracy check of a Taylor vortex-type flow with a force term, a computational result of the flow past a non-symmetric square, and numerical simulation of the flow passing through a complicated region which models

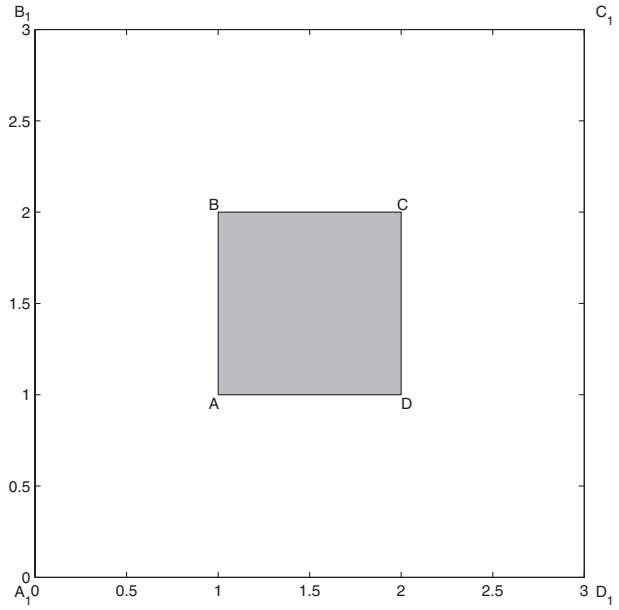

Fig. 2. A multi-connected domain with a single square "hole".

a heat exchanger. We believe the second and third examples give numerical evidence of the robustness of our scheme due to their geometric complexity.

2. The second order scheme

For simplicity of presentation, the following domain with a single square "hole", as shown in Fig. 2, is used to describe the scheme. A domain with an arbitrary number of holes can be dealt with in a similar way, and the corresponding scheme will be discussed in Remark 2.4.

In Fig. 2, $\partial\Omega$ is composed of the outer closed boundary Γ_0: $A_1B_1C_1D_1$ and only one segment Γ_1: $ABCD$, where $A_1B_1C_1D_1$, $ABCD$ are $[0,3]^2$ and $[1,2]^2$ boxes, respectively. In particular, A, B, C, D have grid indices (n,n), (n,m), (m,m), and (m,n), and A_1, B_1, C_1, D_1 have grid indices $(0,0)$, $(0,N)$, (N,N), $(N,0)$, with $n = (1/3)N$, $m = (2/3)N$, respectively. The grid size is chosen as $\Delta x = \Delta y = h$. N_i is the number of interior grid points. $\widetilde{\mathrm{D}}_x$, D_x^2 are the standard centered difference operators corresponding to ∂_x, ∂_x^2, respectively.

The crucial part in the numerical simulation of system (1.5) is the computation of the Poisson equation (1.5b) and the enforcement of boundary conditions (1.5c), (1.5d). We first describe the computational strategy to deal with this part. The Laplacian operator in (1.5b) can be approximated by the second order finite difference operator $\Delta_h = \mathrm{D}_x^2 + \mathrm{D}_y^2$, and the usage of the Dirichlet boundary condition in (1.5c) leads to the following discrete system

$$\begin{cases} \Delta_h \psi = \omega, & \text{in } \Omega, \\ \psi|_{\Gamma_0} = 0, \quad \psi|_{\Gamma_1} = C_1. \end{cases} \tag{2.1}$$

The constant C_1 is not known and the remaining work is to obtain it from boundary condition (1.5d).

The no-slip boundary condition $\partial\psi/\partial\boldsymbol{n} = 0$ can be converted into the boundary condition for the vorticity by a local formula, such as *Thom's* formula proposed in [31]. For example, on the boundary section A_1D_1, $j = 0$, Thom's formula gives

$$\omega_{i,0} = \frac{2\psi_{i,1} - 2\psi_{i,0}}{h^2}, \tag{2.2}$$

and on AD, one boundary section of Γ_1, the corresponding formula indicates

$$\omega_{i,n} = \frac{2\psi_{i,n-1} - 2\psi_{i,n}}{h^2}. \tag{2.3}$$

Similar formulae can be applied to the other boundary sections. A local boundary formula for vorticity is derived from the combination of the kinematic relation $\omega = \Delta\psi$ with the no-slip boundary condition $\partial\psi/\partial\boldsymbol{n} = 0$, using a one-sided approximation and a high order Taylor expansion of the stream function near the boundary. The usage of a local vorticity formula in large Reynolds flow computation was introduced in [7], which made a dramatic difference with the global vorticity boundary formulae appearing in [1,25].

The boundary condition $\int_{\Gamma_1} \partial\omega/\partial\boldsymbol{n} = 0$ can thus be implemented by a finite difference approximation. For the convenience of the presentation below, some notations are introduced.

Notation. For any discrete field f on the grid points (i,j), we define

$$\int_{\Gamma_1}^{(\boldsymbol{k})} f = \int_{AB} f_{n-k,j} + \int_{BC} f_{i,m+k} + \int_{CD} f_{m+k,j} + \int_{DA} f_{i,n-k}, \tag{2.4}$$

where the trapezoidal rule is applied to the integration on each boundary section. For example, on section AB,

$$\int_{AB} f_{n-k,j} = h\left(\frac{1}{2} f_{n-k,n} + \sum_{j=n+1}^{m-1} f_{n-k,j} + \frac{1}{2} f_{n-k,m}\right). \tag{2.5}$$

Using the one-sided difference operator $(4\omega_{n-1,j} - \omega_{n-2,j} - 3\omega_{n,j})/2h$ as a second order approximation to $\partial\omega/\partial\boldsymbol{n}$ (on the boundary section AB), and combining with boundary condition (1.5d) results in

$$\int_{\Gamma_1}^{(\mathbf{0})} \omega = \frac{4}{3}\int_{\Gamma_1}^{(\mathbf{1})} \omega - \frac{1}{3}\int_{\Gamma_1}^{(\mathbf{2})} \omega. \tag{2.6}$$

The substitution of Thom's formula (2.3) into the left-hand side of (2.6), along with the fact that ψ is a constant on the boundary Γ_1, gives

$$C_1 = \frac{1}{|\Gamma_1|}\left(\int_{\Gamma_1}^{(\mathbf{1})} \psi - \frac{2}{3}h^2 \int_{\Gamma_1}^{(\mathbf{1})} \omega + \frac{1}{6}h^2 \int_{\Gamma_1}^{(\mathbf{2})} \omega\right), \tag{2.7}$$

where $|\Gamma_1|$ is the length of the boundary Γ_1. In the case of Fig. 2, $|\Gamma_1| = 4$.

Formula (2.7) plays the role of a bridge between the constant C_1 and the boundary condition $\int_{\Gamma_1} \partial\omega/\partial\boldsymbol{n} = 0$. A different C_1 leads to a different $\psi_{i,j}$, which, in turn, results in a different vorticity ω on the boundary, by Thom's formulae (2.2), (2.3), and to a different $\int_{\Gamma_1} \partial\omega/\partial\boldsymbol{n}$. On the other hand, this integral has to be 0, according to (1.5d).

The coupled system (2.1), (2.7) will be used to compute ψ and the constant C_1 by iteration, as will be explained in detail later. There are $N_i + 1$ unknowns (where N_i is the number of interior grid points), including N_i number of $\psi_{i,j}$ at interior grid points and the boundary value C_1; the number of equations is also $N_i + 1$: N_i equations in (2.1) and the additional equation (2.7).

As argued above, the right-hand side of (2.7) depends on C_1. An operator ϕ can be introduced by (2.7). For any constant C, denote ψ to be the solution of the system

$$\begin{cases} \Delta_h \psi = \omega, & \text{in } \Omega, \\ \psi|_{\Gamma_0} = 0, \quad \psi|_{\Gamma_1} = C, \end{cases} \tag{2.8}$$

and define

$$\phi(C) = \frac{1}{|\Gamma_1|}\left(\int_{\Gamma_1}^{(\mathbf{1})} \psi - \frac{2}{3}h^2 \int_{\Gamma_1}^{(\mathbf{1})} \omega + \frac{1}{6}h^2 \int_{\Gamma_1}^{(\mathbf{2})} \omega\right). \tag{2.9}$$

It should be noted that the term related to ψ on the right-hand side of (2.9) depends on C, according to (2.8). Obviously, the fixed point of ϕ, i.e., the constant C such that $\phi(C) = C$, along with ψ determined by (2.8), is exactly the solution of the coupled system (2.1), (2.7). The existence and uniqueness of the fixed point can be guaranteed by the following proposition, which states that ϕ is a contraction mapping.

Proposition 2.1. *For any* $C_1, C_2 \in R$, *we have*

$$|\phi(C_1) - \phi(C_2)| \leqslant C^*|C_1 - C_2|, \quad \text{where } C^* = 1 - h. \tag{2.10}$$

Proof. Denote by ψ^1, ψ^2 the solutions of system (2.8) with boundary conditions $\psi^1|_{\Gamma_1} = C_1$, $\psi^2|_{\Gamma_1} = C_2$, respectively. Define $\widetilde{\psi} = \psi^1 - \psi^2$. It can be seen that

$$\begin{cases} \Delta_h \widetilde{\psi} = 0, & \text{in } \Omega, \\ \widetilde{\psi}|_{\Gamma_0} = 0, & \widetilde{\psi}|_{\Gamma_1} = C_1 - C_2. \end{cases} \tag{2.11}$$

The definition of $\phi(C_1)$ and $\phi(C_2)$, which was indicated by (2.9), gives

$$\phi(C_1) - \phi(C_2) = \frac{1}{|\Gamma_1|} \int_{\Gamma_1}^{(1)} \widetilde{\psi}. \tag{2.12}$$

The estimate of the right side of (2.12) is obtained by the following lemma.

Lemma 2.2. *Let* u *be the solution of the system*

$$\begin{cases} \Delta_h u = 0, & \text{in } \Omega, \\ u|_{\Gamma_0} = 0, & u|_{\Gamma_1} = 1, \end{cases} \tag{2.13}$$

then we have

$$0 \leqslant u_{n-1,j} \leqslant C^*, \quad \text{for } n \leqslant j \leqslant m, \quad \text{where} \quad C^* = 1 - h. \tag{2.14}$$

Proof. The first part of (2.14) comes directly from the maximum principle of the discrete Laplacian operator Δ_h. For the second part, the region Ω can be partitioned into four sub-regions: A_1ABB_1, A_1ADD_1, D_1DCC_1, C_1CBB_1, denoted by Ω_1, Ω_2, Ω_3, Ω_4, respectively, as shown in Fig. 3.

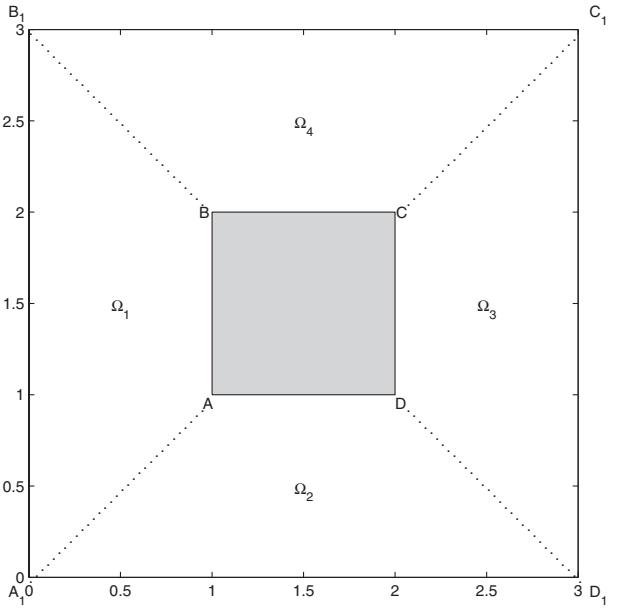

Fig. 3. A partition of the domain.

Clearly, the function

$$v = \begin{cases} x, & \text{in } \Omega_1, \\ y, & \text{in } \Omega_2, \\ 3 - x, & \text{in } \Omega_3, \\ 3 - y, & \text{in } \Omega_4, \end{cases} \tag{2.15}$$

satisfies

$$\begin{cases} \Delta_h v = \begin{cases} -\frac{2}{h}, & \text{on } AA_1, BB_1, CC_1, DD_1, \\ 0, & \text{otherwise}, \end{cases} \\ v|_{\Gamma_0} = 0, \quad v|_{\Gamma_1} = 1. \end{cases} \tag{2.16}$$

Denote $f = -\Delta_h v$. Obviously, $f \geqslant 0$. Then u can be decomposed into two parts: $u = v + w$, where w is the solution of the following system

$$\begin{cases} \Delta_h w = f, & \text{in } \Omega, \\ w|_{\Gamma_0} = 0, & w|_{\Gamma_1} = 0. \end{cases} \tag{2.17}$$

Since $\Delta_h w = f \geqslant 0$, and w vanishes on the boundary, from the maximum principle of Δ_h we have $w \leqslant 0$ at all grid points. Then we arrive at

$$u \leqslant v, \quad \text{at all grid points}, \tag{2.18}$$

and in particular, $u_{n-1,j} \leqslant v_{n-1,j} = 1 - h = C^*$. □

It is obvious that $\widetilde{\psi} = (C_1 - C_2)u$ where u is given in Lemma 2.2. This results in

$$|\widetilde{\psi}_{n-1,j}| \leqslant C^* |C_1 - C_2|, \quad \text{for } n \leqslant j \leqslant m. \tag{2.19}$$

Similar arguments can be used to estimate $\widetilde{\psi}_{i,m+1}$, $\widetilde{\psi}_{m+1,j}$, $\widetilde{\psi}_{i,n-1}$. Proposition 2.1 is a direct consequence of (2.19) and (2.12). □

According to Proposition 2.1, there is an unique fixed point under the operator ϕ, i.e., $\phi(C) = C$. That is exactly the solution of system (2.1), (2.7). Thus the existence and uniqueness of the system is proven.

Remark 2.3. The other choices for the vorticity boundary condition include *Wilkes*' formulae

$$\omega_{i,0} = \frac{4\psi_{i,1} - \frac{1}{2}\psi_{i,2} - \frac{7}{2}\psi_{i,0}}{h^2}, \quad \omega_{i,n} = \frac{4\psi_{i,n-1} - \frac{1}{2}\psi_{i,n-2} - \frac{7}{2}\psi_{i,n}}{h^2}, \tag{2.20}$$

which are analogous to (2.2), (2.3). Note that Wilkes' formula is also a local boundary formula for the vorticity field. Therefore, the approach using the explicit treatment of the diffusion term introduced in [7] can be used very effectively. The combination of (2.6), (2.20) gives the corresponding formula for C_1

$$C_1 = \frac{1}{|\Gamma_1|}\left(\frac{8}{7}\int_{\Gamma_1}^{(1)} \psi - \frac{1}{7}\int_{\Gamma_1}^{(1)} \psi - \frac{8}{21}h^2 \int_{\Gamma_1}^{(1)} \omega + \frac{2}{21}h^2 \int_{\Gamma_1}^{(2)} \omega\right). \tag{2.21}$$

Again, the coupled system (2.1), (2.21) has to be solved to obtain ψ and the constant C_1 by an iterative method. The existence of the solution can be guaranteed by introducing a similar contraction mapping ϕ: for any constant C, denote ψ to be the solution of (2.8), and define

$$\phi(C) = \frac{1}{|\Gamma_1|}\left(\frac{8}{7}\int_{\Gamma_1}^{(1)}\psi - \frac{1}{7}\int_{\Gamma_1}^{(1)}\psi - \frac{8}{21}h^2\int_{\Gamma_1}^{(1)}\omega + \frac{2}{21}h^2\int_{\Gamma_1}^{(2)}\omega\right). \tag{2.22}$$

Proposition 2.1 is still valid here. The only difference is that $C^* = 1 - (6/7)h + \mathrm{O}(h^2)$. It should be mentioned that C^* is the convergence rate corresponding to different vorticity boundary conditions. For example, $1 - h$ is the convergence rate for Thom's formula, and $1 - (6/7)h$ is the convergence rate for Wilkes' formula. The detailed derivation of convergence rates comes from a simple 1-D model. This convergence rate is consistent with the numerical experiments which will be presented in Section 4.

Remark 2.4. A general region with an arbitrary number of holes can be handled in the same way. An iterative formula, either (2.7) or (2.21), can be applied on each boundary section Γ_i. In more detail, with an initial guess for the boundary values of ψ on each Γ_i, the formula provides a methodology to determine the constants on all boundary sections. We provide the convergence analysis for the multi-connected domain with a single square "hole" (such as in Fig. 2) using the technique relying on the maximum principle and contraction mapping. It is not our purpose to give a complete proof for a general domain. It may be an extremely difficult task. Our expectation is that this simple iterative procedure can be used in a more complicated domain with more than one immersed body, as shown in Figs. 14–21 of the computational results for a flow past a heat exchanger.

Proposition 2.1 also provides a methodology for solving the system (2.1), (2.7) by an iterative procedure: once the kth iteration for the constant $C_1^{(k)}$ is obtained, solve the stream function $\psi^{(k)}$ using the boundary condition $C_1^{(k)}$, then update the constant $C_1^{(k+1)}$ by the $(k+1)$th iteration: $C_1^{(k+1)} = \phi(C_1^{(k)})$. Proposition 2.1 indicates that this iterative procedure converges to the exact solution of (2.1), (2.7).

It should be pointed out that with the constant $C_1^{(k)}$ obtained at each iteration stage, a linear system solver for (2.1) is required. The Schwarz iteration is extremely efficient to solve this (discrete) Poisson equation in an overlapping region. At each sub-domain, which is a rectangle with uniform grid, some fast Poisson solvers, e.g., FFT, can be applied. The computational evidence indicates that the combination of the Schwarz iteration and FFT solver has an excellent convergence property in the overlapping region.

The momentum equation in (1.5a) can be discretized by the second order finite difference method

$$\partial_t\omega + u\,\widetilde{\mathbf{D}}_x\omega + v\,\widetilde{\mathbf{D}}_y\omega = \nu\,\Delta_h\omega. \tag{2.23}$$

The velocity field $\boldsymbol{u} = (u, v) = (-\partial_y\psi, \partial_x\psi)$ can be updated via the finite difference of ψ

$$u = -\widetilde{\mathbf{D}}_y\psi, \quad v = \widetilde{\mathbf{D}}_x\psi. \tag{2.24}$$

2.1. Time stepping procedure

Since the focus of this article is large Reynolds number flow calculations, the above scheme can be implemented very effectively through the explicit treatment of (2.23). The convection and diffusion terms can be updated explicitly, which does not result in any problem caused by the cell-Reynolds number constraint if a high order time stepping procedure, such as the fourth order Runge–Kutta method, is applied. Such an explicit treatment is especially effective in the Poisson solver (2.1), (2.7) when we apply the iterative formula to determine the unknown constant(s) for the stream function on the boundary. In turn, the vorticity boundary condition can be obtained by a local formula, either Thom's (2.2) or Wilkes' (2.20).

For simplicity, we only present the forward Euler time discretization. The extension to multi-step or Runge–Kutta methods is straightforward.

Given the vorticity ω^n at time t^n, we compute all the profiles at the time step t^{n+1} via the following steps.

Step 1. Update $\{\omega_{i,j}^{n+1}\}$, at the interior points (x_i, y_j), using

$$\frac{\omega^{n+1}-\omega^n}{\Delta t} + u^n \widetilde{\mathbf{D}}_x \omega^n + v^n \widetilde{\mathbf{D}}_y \omega^n = \nu \Delta_h \omega^n. \tag{2.25}$$

Step 2. Solve for $\{\psi_{i,j}^{n+1}\}$, at the interior points (x_i, y_j), by the following coupled system

$$\begin{cases} \Delta_h \psi^{n+1} = \omega^{n+1}, & \text{in } \Omega, \\ \psi^{n+1}|_{\Gamma_0} = 0, \quad \psi^{n+1}|_{\Gamma_1} = C_1^{n+1}, \end{cases} \tag{2.26}$$

and

$$C_1^{n+1} = \frac{1}{|\Gamma|}\left(\int_{\Gamma_1}^{(1)} \psi^{n+1} - \frac{2}{3}h^2 \int_{\Gamma_1}^{(1)} \omega^{n+1} + \frac{1}{6}h^2 \int_{\Gamma_1}^{(2)} \omega^{n+1} \right). \tag{2.27}$$

The iterative procedure described above is used to solve (2.26), (2.27).

Step 3. Obtain the boundary value for ω^{n+1} by Thom's formulae (2.2) and (2.3).

Step 4. Update the velocity $u_{i,j}^{n+1}$, $v_{i,j}^{n+1}$, using the second order difference scheme

$$u^{n+1} = -\widetilde{\mathbf{D}}_y \psi^{n+1}, \quad v^{n+1} = \widetilde{\mathbf{D}}_x \psi^{n+1}, \tag{2.28}$$

at interior grid points, and $u^{n+1}|_{\partial\Omega} = 0, v^{n+1}|_{\partial\Omega} = 0$.

As for the time step constraint, the overall scheme is stable as long as Δt satisfies

$$\frac{\|\boldsymbol{u}\|_\infty \Delta t}{h} \leqslant \mathrm{CFL} \leqslant 1.0 \quad \text{and} \quad \frac{\nu \Delta t}{h^2} \leqslant \frac{1}{4}. \tag{2.29}$$

See [7,32] for a detailed discussion of issues concerning the choice of the time stepping scheme and stability conditions.

3. The fourth order method

A fourth order method, the essentially compact fourth order scheme, which was proposed in [8], is used in this section. The starting idea of the scheme is the fourth order compact approximation to the Laplacian operator Δ

$$\Delta = \frac{\Delta_h + \frac{h^2}{6}\mathrm{D}_x^2\mathrm{D}_y^2}{1 + \frac{h^2}{12}\Delta_h} + \mathrm{O}(h^4). \tag{3.1}$$

Multiplying the denominator difference operator $1 + (h^2/12)\Delta_h$ by the momentum equation gives

$$\left(1 + \frac{h^2}{12}\Delta_h\right)\partial_t\omega + \left(1 + \frac{h^2}{12}\Delta_h\right)(\boldsymbol{u}\cdot\nabla)\omega = \nu\left(\Delta_h + \frac{h^2}{6}\mathrm{D}_x^2\mathrm{D}_y^2\right)\omega. \tag{3.2}$$

Multiplying the same operator by the kinematic equation results in

$$\left(\Delta_h + \frac{h^2}{6}\mathrm{D}_x^2\mathrm{D}_y^2\right)\psi = \left(1 + \frac{h^2}{12}\Delta_h\right)\omega, \tag{3.3}$$

with the boundary conditions

$$\psi|_{\Gamma_0} = 0, \quad \psi|_{\Gamma_1} = C_1. \tag{3.4}$$

As in the second order case, the constant C_1 is not known yet, and can be obtained from the boundary condition in (1.5d).

The implementation of the boundary condition $\int_{\Gamma_1}\partial\omega/\partial\boldsymbol{n} = 0$ is performed a little differently than in the second order case. As can be seen later, the vorticity in the interior points has to be determined by a Poisson-like equation. The boundary condition for ω, which in turn depends on the stream function and C_1, can be determined by Briley's formula, which will be presented later. To avoid coupling between the two systems, we express $\partial\omega/\partial\boldsymbol{n}$ in terms of a third order derivative of ψ, which can facilitate the computations, as shown in our numerical experiments. On the boundary section AD of Γ_1, $\omega = \Delta\psi = \partial_y^2\psi$, which is implied by the fact that $\psi = C_1$ on AD. Furthermore, we have $\partial\omega/\partial\boldsymbol{n} = -\partial_y^3\psi$ on AD since $\partial_y\partial_x^2\psi$ vanishes on the boundary. On the other hand, ∂_y^3 can be approximated by

$$\partial_y^3\psi_{i,n} \sim \frac{1}{h^3}(15\psi_{i,n-1} - 6\psi_{i,n-2} + \psi_{i,n-3} - 10\psi_{i,n}). \tag{3.5}$$

The third order derivative of ψ on the other boundary sections of Γ_1 can be obtained similarly. Inserting (3.5) into the boundary condition $\int_{\Gamma_1}\partial\omega/\partial\boldsymbol{n} = 0$, we arrive at an equality similar to (2.6)

$$\int_{\Gamma_1}^{(\mathbf{0})}\psi = \frac{3}{2}\int_{\Gamma_1}^{(\mathbf{1})}\psi - \frac{3}{5}\int_{\Gamma_1}^{(\mathbf{2})}\psi + \frac{1}{10}\int_{\Gamma_1}^{(\mathbf{3})}\psi. \tag{3.6}$$

Since ψ is a constant C_1 on Γ_1, we have

$$C_1 = \frac{3}{2|\Gamma_1|}\int_{\Gamma_1}^{(\mathbf{1})}\psi - \frac{3}{5|\Gamma_1|}\int_{\Gamma_1}^{(\mathbf{2})}\psi + \frac{1}{10|\Gamma_1|}\int_{\Gamma_1}^{(\mathbf{3})}\psi. \tag{3.7}$$

Again, formula (3.7) plays the role of a bridge between the constant C_1 and the boundary condition $\int_{\Gamma_1} \partial\omega/\partial \boldsymbol{n} = 0$. Different C_1's lead to different $\psi_{i,j}$'s, which in turn result in different values of $\int_{\Gamma_1} \partial\omega/\partial \boldsymbol{n}$, while (1.5d) indicates that this integral has to be 0.

The coupled system (3.3), (3.4), (3.7) is used to obtain ψ and the constant C_1 by an iterative scheme. A similar argument shows that the number of both equations and unknowns is $N_i + 1$.

The right-hand side of (3.7) clearly depends on C_1 and a similar iterative procedure can be applied. First, we define the operator ϕ: for any constant C, let ψ be the solution satisfying

$$\begin{cases} \left(\Delta_h + \frac{h^2}{6} \mathrm{D}_x^2 \mathrm{D}_y^2\right)\psi = \left(1 + \frac{h^2}{12}\Delta_h\right)\omega, \\ \psi|_{\Gamma_0} = 0, \quad \psi|_{\Gamma_1} = C, \end{cases} \tag{3.8}$$

and $\phi(C)$ is defined by

$$\phi(C) = \frac{3}{2|\Gamma_1|}\int_{\Gamma_1}^{(1)} \psi - \frac{3}{5|\Gamma_1|}\int_{\Gamma_1}^{(2)} \psi + \frac{1}{10|\Gamma_1|}\int_{\Gamma_1}^{(3)} \psi. \tag{3.9}$$

The following proposition shows that ϕ is a contraction mapping. Its proof is similar to that of Proposition 2.1 in the second order case and will be provided in Appendix A.

Proposition 3.1. *For any two constants C_1, C_2, we have*

$$|\phi(C_1) - \phi(C_2)| \leqslant C^*|C_1 - C_2|, \quad \textit{where } C^* = 1 - \mathrm{O}(h). \tag{3.10}$$

By Proposition 3.1, there is a fixed point for the operator ϕ, i.e., $\phi(C) = C$, which is exactly the solution of system (3.3), (3.4), (3.7). Thus the existence and uniqueness of the system is proven.

A similar method for solving system (3.3), (3.4), (3.7) can be obtained from the following iterative procedure: once the kth iteration for the constant $C_1^{(k)}$ is obtained, solve for the stream function $\psi^{(k)}$ using the boundary condition as $C = C_1^{(k)}$ in (3.8), then update the constant $C_1^{(k+1)}$ by the $(k+1)$th iteration: $C_1^{(k+1)} = \phi(C_1^{(k)})$. This iteration procedure converges to the exact solution of (3.3), (3.4), (3.7), as was guaranteed by Proposition 3.1.

Remark 3.2. A general region with an arbitrary number of holes can be treated in a similar way. We apply the iterative formula (3.7) on each boundary section Γ_i, so that the constants on all boundary sections can be determined by an iterative procedure.

The corresponding non-linear convection term in the vorticity transport equation can be estimated as

$$\begin{aligned} \left(1 + \frac{h^2}{12}\Delta_h\right)(\boldsymbol{u}\cdot\nabla\omega) = \widetilde{\mathrm{D}}_x\left(1 + \frac{h^2}{6}\mathrm{D}_y^2\right)(u\omega) + \widetilde{\mathrm{D}}_y\left(1 + \frac{h^2}{6}\mathrm{D}_x^2\right)(v\omega) - \frac{h^2}{12}\Delta_h(u\,\widetilde{\mathrm{D}}_x\omega \\ + v\,\widetilde{\mathrm{D}}_y\omega) + \mathrm{O}(h^4). \end{aligned} \tag{3.11}$$

The first and second terms in (3.11) are compact. The third term is not compact, yet it does not cause any problem in the computations since $u^n\,\widetilde{\mathrm{D}}_x\omega^n + v^n\,\widetilde{\mathrm{D}}_y\omega^n$ can be taken as 0 on the boundary. The case of a boundary condition with a slip can be treated similarly. Finally, by introducing an intermediate variable $\overline{\omega}$

$$\overline{\omega} = \left(1 + \frac{h^2}{12}\Delta_h\right)\omega, \tag{3.12}$$

and combining the discussions in (3.2), (3.11), (3.12), the momentum equation can be approximated by

$$\begin{aligned}&\partial_t\overline{\omega} + \widetilde{\mathbf{D}}_x\left(1 + \frac{h^2}{6}\mathrm{D}_y^2\right)(u\omega) + \widetilde{\mathbf{D}}_y\left(1 + \frac{h^2}{6}\mathrm{D}_x^2\right)(v\omega) - \frac{h^2}{12}\Delta_h(u\,\widetilde{\mathbf{D}}_x\omega + v\,\widetilde{\mathbf{D}}_y\omega)\\ &\quad = v\left(\Delta_h + \frac{h^2}{6}\mathrm{D}_x^2\mathrm{D}_y^2\right)\omega.\end{aligned} \tag{3.13}$$

The velocity field $\boldsymbol{u} = \nabla^\top\psi = (-\partial_y\psi, \partial_x\psi)$ can be obtained by a long-stencil approximation to ∂_x, ∂_y

$$u = -\widetilde{\mathbf{D}}_y\left(1 - \frac{h^2}{6}\mathrm{D}_y^2\right)\psi, \quad v = \widetilde{\mathbf{D}}_x\left(1 - \frac{h^2}{6}\mathrm{D}_x^2\right)\psi. \tag{3.14}$$

The vorticity is determined by $\overline{\omega}$ via (3.12). The implementation of (3.12) requires the boundary condition for ω. The key point of the vorticity boundary condition is to use the no-slip boundary condition $\partial\psi/\partial\boldsymbol{n} = 0$, and convert it to $\omega|_{\partial\Omega}$ by the kinematic relation $\Delta\psi = \omega$. We can use Briley's formula (proposed in [3])

$$\omega_{i,0} = \frac{1}{18h^2}(108\psi_{i,1} - 27\psi_{i,2} + 4\psi_{i,3} - 85\psi_{i,0}), \tag{3.15}$$

along with the one-sided Taylor expansions of the stream function

$$\psi_{i,-1} = 6\psi_{i,1} - 2\psi_{i,2} + \frac{1}{3}\psi_{i,3} - \frac{10}{3}\psi_{i,0} - 4h\left(\frac{\partial\psi}{\partial y}\right)_{i,0}, \tag{3.16}$$

$$\psi_{i,-2} = 40\psi_{i,1} - 15\psi_{i,2} + \frac{8}{3}\psi_{i,3} - \frac{80}{3}\psi_{i,0} - 12h\left(\frac{\partial\psi}{\partial y}\right)_{i,0}. \tag{3.17}$$

On the boundary section AD, Briley's formula gives

$$\omega_{i,n} = \frac{1}{18h^2}(108\psi_{i,n-1} - 27\psi_{i,n-2} + 4\psi_{i,n-3} - 85\psi_{i,n}). \tag{3.18}$$

It should be mentioned that system (3.12) and boundary conditions (3.15), (3.18) can be solved very efficiently by the combination of the Schwarz iteration and FFT solver.

The temporal discretization is similar to that of the second order scheme presented in Section 2. All terms in the momentum equation can be updated explicitly. Such an explicit treatment makes the Poisson solver (3.3), (3.4), (3.7) very efficient. In turn, the vorticity is calculated on the boundary by Briley's formula (3.15). For conciseness of the article we omit the detail.

4. Numerical experiments

Three numerical examples will be presented to show the robustness of the methods proposed above. The first example is a flow with a force term. The accuracy of both the second order and fourth order methods is established. The second example is flow past a non-symmetric square cylinder. The third example is flow passing through a complicated region which models a heat exchanger. Detailed structures of the vorticity at different time steps are given. Comparison of three resolutions will also be given, indicating a good agreement.

4.1. Accuracy check

A Taylor vortex-type flow in a multi-connected domain is computed by the methods proposed earlier. The exact stream function is chosen as

$$\psi_e v(\boldsymbol{x}, t) = (\cos x + \cos y + \cos x \cos y)\cos t. \tag{4.1}$$

Accordingly, the exact velocity and vorticity are determined by

$$\begin{aligned} u_e(\boldsymbol{x}, t) &= -\partial_y \psi_e = (\sin y + \cos x \sin y)\cos t, \\ v_e(\boldsymbol{x}, t) &= \partial_x \psi_e = (-\sin x - \sin x \cos y)\cos t, \\ \omega_e(\boldsymbol{x}, t) &= \Delta \psi_e = (-\cos x - \cos y - 2\cos x \cos y)\cos t. \end{aligned} \tag{4.2}$$

The kinematic viscosity is taken as $\nu = 0.001$. Substitution of (4.2) into the momentum equation gives

$$\partial_t \omega_e + (\boldsymbol{u}_e \cdot \nabla)\omega_e = \nu \Delta \omega_e + \boldsymbol{f}, \tag{4.3}$$

where $\boldsymbol{f}$ is the force term. The domain has the same shape as in Fig. 2. The dimensions of the boxes $A_1B_1C_1D_1$ and $ABCD$ are $[-3\pi, 3\pi]^2$ and $[-\pi, \pi]^2$, respectively. Using the same notation as before, we denote the outer boundary $A_1B_1C_1D_1$ by Γ_0, and the inner boundary $ABCD$ by Γ_1. It is obvious that the boundary condition for stream function on the outer boundary is

$$\psi(\boldsymbol{x}, t)|_{\Gamma_0} = -\cos t, \tag{4.4}$$

which is a constant varying with time t. Stream function is also a constant on Γ_1, (at each fixed time), denoted by C_1. Yet, C_1 is not explicitly utilized in the computation. Instead, we need to obtain this constant by the procedure described in Sections 2 and 3.

4.1.1. Second order scheme

Eq. (4.3) can be solved via our second order method coupled with the fourth order Runge–Kutta time discretization, as discussed in (2.25)–(2.28). Wilkes' formula (2.20) is chosen as the boundary condition for the vorticity and the recovery formula (2.21) is applied to determine the boundary value of the stream function on Γ_1. The force term $\boldsymbol{f}$ is added when (4.3) is updated. We investigate the computed solution at $t = 2.0$, 4.0, 6.0, respectively. The time step size is taken as $\Delta t = (1/2)\Delta x$, so that the stability constraint (2.29) is satisfied (noting that $\|\boldsymbol{u}\|_\infty = 1$, $\nu = 0.001$ in the present case). The absolute errors in the stream function and vorticity at $t = 2.0$, 4.0 and 6.0 are listed in Tables 1–3, respectively. As can be seen, the computed solution of the stream function is second order accurate almost exactly, while that of the vorticity is second order accurate in the

Table 1
Errors and orders of accuracy at $t = 2$ when the second order method, which was described in Section 2, is used. We take $\Delta t = (1/2)\Delta x$

	N	L^1 error	L^1 order	L^2 error	L^2 order	L^∞ error	L^∞ order
ψ	72	3.65e−03		4.60e−03		1.09e−02	
	96	1.82e−03	2.42	2.35e−03	2.33	5.76e−03	2.22
	144	7.18e−04	2.29	9.64e−04	2.20	2.41e−03	2.15
	192	3.82e−04	2.19	5.22e−04	2.13	1.32e−03	2.09
	288	1.72e−04	1.98	2.40e−04	1.93	6.16e−04	1.90
ω	72	3.66e−03		5.57e−03		4.01e−02	
	96	2.02e−03	2.06	3.20e−03	1.93	2.90e−02	1.13
	144	8.83e−04	2.04	1.45e−03	1.95	1.69e−02	1.33
	192	4.95e−04	2.01	8.04e−04	2.05	1.06e−02	1.62
	288	2.21e−04	1.99	3.45e−04	2.08	4.71e−03	2.00

Table 2
Errors and orders of accuracy at $t = 4$ when the second order method, which was described in Section 2, is used. We take $\Delta t = (1/2)\Delta x$

	N	L^1 error	L^1 order	L^2 error	L^2 order	L^∞ error	L^∞ order
ψ	72	5.18e−03		6.80e−03		1.74e−02	
	96	2.92e−03	1.99	3.81e−03	2.01	9.64e−03	2.05
	144	1.23e−03	2.13	1.58e−03	2.17	3.94e−03	2.21
	192	7.01e−04	1.96	9.03e−04	1.95	2.24e−03	1.96
	288	3.05e−04	2.05	3.92e−04	2.06	9.71e−04	2.06
ω	72	8.32e−03		1.20e−02		7.47e−02	
	96	4.55e−03	2.10	6.87e−03	1.93	5.58e−02	1.01
	144	1.96e−03	2.08	3.14e−03	1.93	3.43e−02	1.20
	192	1.10e−03	2.01	1.79e−03	1.95	2.27e−02	1.43
	288	4.90e−04	2.00	7.98e−04	1.99	1.12e−02	1.74

Table 3
Errors and orders of accuracy at $t = 6$ when the second order method, which was described in Section 2, is used. We take $\Delta t = (1/2)\Delta x$

	N	L^1 error	L^1 order	L^2 error	L^2 order	L^∞ error	L^∞ order
ψ	72	8.47e−03		1.08e−02		2.68e−02	
	96	4.36e−03	2.31	5.73e−03	2.20	1.44e−02	2.16
	144	1.73e−03	2.28	2.34e−03	2.21	5.93e−03	2.19
	192	9.34e−04	2.14	1.28e−03	2.10	3.27e−03	2.07
	288	3.98e−04	2.10	5.52e−04	2.07	1.42e−03	2.06
ω	72	9.58e−03		1.48e−02		1.10e−01	
	96	5.34e−03	2.03	8.63e−03	1.87	7.74e−02	1.22
	144	2.30e−03	2.08	3.80e−03	2.02	4.14e−02	1.54
	192	1.30e−03	1.98	2.18e−03	1.93	2.60e−02	1.62
	288	5.78e−04	2.00	9.95e−04	1.94	1.42e−02	1.50

L^1 and L^2 norms, and obviously loses full accuracy in the L^∞ norm. All the errors are measured in the L^1, L^2 and L^∞ norms, with the L^p norm defined by

$$\|f\|_{L^p} = \left(\frac{1}{|\Omega|} \int_\Omega |f|^p \, d\boldsymbol{x} \right)^{1/p}, \quad \text{for } 1 \leqslant p \leqslant \infty, \tag{4.5}$$

where $|\Omega| = 32\pi^2$ in this case. The numerical solution f is extended to a piecewise constant function over the whole region Ω in the evaluation of (4.5).

The observation of the loss of accuracy in the L^∞ norm for the vorticity profile is interesting. For a simply connected domain, it is reported in an earlier article [32] that full second order accuracy is obtained for all the computed profiles in both the L^1, L^2 and L^∞ norms. Theoretical analysis of second order convergence was also established in [14,32]. Such an analysis for the whole non-linear system is available, since the stream function value is exactly given on all boundary sections. In contrast, formula (2.7) or (2.21) only gives a second order approximation to the value of the stream function on the boundary section of the hole, by utilizing a finite difference. Moreover, in the vorticity boundary formula (2.20), there is a singular coefficient $O(1/h^2)$. We believe the above issues are the main reason for the loss of accuracy in the L^∞ norm for the vorticity.

4.1.2. Fourth order scheme

The fourth order method coupled with the fourth order Runge–Kutta time discretization can also be used to compute the flow. The force term which will be added to the vorticity equation (4.3) becomes $(1 + (h^2/12)\Delta_h)\boldsymbol{f}$, since we applied the operator $1 + (h^2/12)\Delta_h$ to the momentum equation. The time step size is also taken to be $\Delta t = (1/2)\Delta x$ so that the stability constraint (2.29) is valid. The absolute errors in the stream function and vorticity at $t = 2.0$, 4.0 and 6.0 are listed in Tables 4–6, respectively. From the tables, it can be seen that more than fourth order accuracy is obtained for the computed solution of the stream function in the L^1, L^2 and L^∞ norms. The computed vorticity is fourth order accurate in L^1 and L^2 norms, and more than third order accuracy is obtained in the L^∞ norm.

Once again, the loss of full fourth order accuracy in the L^∞ norm for the vorticity profile can be observed. The reason is believed to be similar to that in the second order scheme.

4.2. Flow past a non-symmetric square cylinder

In this sub-section we justify the proposed numerical method by considering a well-known example of the flow past a cylinder square. A relevant discussion of this physical problem can be found in some earlier literature. For example, experiments of vortex-shedding frequencies of rectangular cylinders were reported in [21]. The main focus was on the Strouhal number and velocity distributions, regarding the long time behavior. In this article, we are mainly concerned with the unsteady flow calculation in a multi-connected domain, in which the boundary value for the stream function at each boundary section of the "hole" needs to be determined by a numerical iterative procedure. Accordingly, we take the following region as shown in Fig. 4 as the computational domain, where the square [1/3, 7/12] × [13/24, 19/24] is located within the [0,2] × [0,1]

Table 4
Errors and orders of accuracy at $t = 2$ when the fourth order method, along with *Briley's Formula* is used. We take $\Delta t = (1/2)\Delta x$

	N	L^1 error	L^1 order	L^2 error	L^2 order	L^∞ error	L^∞ order
ψ	72	6.76e−05		8.51e−05		2.30e−04	
	96	1.70e−05	4.80	2.12e−05	4.83	5.90e−05	4.73
	144	2.54e−06	4.69	3.20e−06	4.66	8.72e−06	4.72
	192	7.10e−07	4.43	9.13e−07	4.36	2.63e−06	4.17
	288	1.44e−07	3.94	1.85e−07	3.94	5.47e−07	3.90
ω	72	1.87e−04		2.73e−04		2.05e−03	
	96	5.67e−05	4.15	8.62e−05	4.01	7.72e−04	3.39
	144	1.07e−05	4.11	1.67e−05	4.05	1.76e−04	3.65
	192	3.39e−06	4.00	5.14e−06	4.09	5.67e−05	3.94
	288	6.73e−07	3.99	1.01e−06	4.01	1.19e−05	3.85

Table 5
Errors and orders of accuracy at $t = 4$ when the fourth order method, along with *Briley's Formula* is used. We take $\Delta t = (1/2)\Delta x$

	N	L^1 error	L^1 order	L^2 error	L^2 order	L^∞ error	L^∞ order
ψ	72	1.89e−04		2.41e−04		6.87e−04	
	96	4.89e−05	4.70	6.26e−05	4.69	1.85e−04	4.56
	144	7.78e−06	4.53	1.01e−05	4.50	3.12e−05	4.39
	192	2.28e−06	4.27	2.96e−06	4.27	9.11e−06	4.28
	288	4.28e−07	4.13	5.56e−07	4.12	1.68e−06	4.17
ω	72	4.56e−04		6.94e−04		4.66e−03	
	96	1.36e−04	4.21	2.19e−04	4.01	1.88e−03	3.16
	144	2.52e−05	4.16	4.22e−05	4.06	4.59e−04	3.48
	192	7.83e−06	4.06	1.30e−05	4.09	1.75e−04	3.35
	288	1.53e−06	4.03	2.48e−06	4.09	4.34e−05	3.44

Table 6
Errors and orders of accuracy at $t = 6$ when the fourth order method, which was described in Section 3, is used. We take $\Delta t = (1/2)\Delta x$

	N	L^1 error	L^1 order	L^2 error	L^2 order	L^∞ error	L^∞ order
ψ	72	1.90e−04		2.40e−04		6.24e−04	
	96	5.08e−05	4.58	6.41e−05	4.59	1.72e−04	4.48
	144	7.76e−06	4.63	9.74e−06	4.65	2.70e−05	4.57
	192	2.18e−06	4.41	2.74e−06	4.41	7.59e−06	4.41
	288	3.81e−07	4.30	4.79e−07	4.30	1.29e−06	4.37
ω	72	5.01e−04		7.52e−04		5.70e−03	
	96	1.57e−04	4.03	2.49e−04	3.85	2.22e−03	3.28
	144	2.92e−05	4.15	4.82e−05	4.05	5.12e−04	3.62
	192	9.24e−06	4.00	1.59e−05	3.86	2.02e−04	3.23
	288	1.79e−06	4.05	3.18e−06	3.97	4.97e−05	3.46

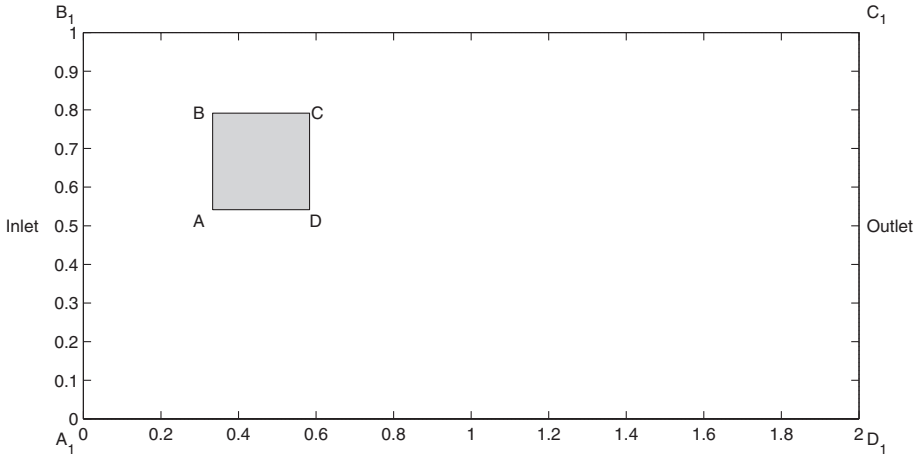

Fig. 4. The region of a flow past a non-symmetric square.

box. Since the domain is non-symmetric, the stream function value on $ABCD$ cannot be obtained directly. Therefore, constraint (1.5d) has to be utilized.

The flow is assumed to be impulsively started. At the inlet A_1B_1, the velocity field is given by the standard parabolic profile

$$u = 6y(1-y), \quad v = 0. \tag{4.6}$$

From the relationship between the velocity and the stream function $\boldsymbol{u} = \nabla^{\perp}\psi$, we can integrate the velocity field at the inlet and set the boundary condition for ψ as:

$$\text{On } A_1B_1, \quad \psi_{\mathrm{b}} = -3y^2 + 2y^3 + 0.5. \tag{4.7}$$

The no-penetration, no-slip boundary condition is imposed at the top (B_1C_1) and bottom (A_1D_1) boundary sections, along with the square $ABCD$. To be consistent with (4.7), the boundary values for ψ at the top and bottom are taken to be $\psi|_{y=0} = 0.5$, $\psi|_{y=1} = -0.5$, respectively. At the outlet C_1D_1, we use the natural normal boundary conditions

$$\text{On } C_1D_1, \qquad \frac{\partial \psi}{\partial \boldsymbol{n}} = 0, \quad \frac{\partial \boldsymbol{u}}{\partial \boldsymbol{n}} = 0, \quad \frac{\partial \omega}{\partial \boldsymbol{n}} = 0. \tag{4.8}$$

The Reynolds number is taken as $Re = (UH)/\nu = 250$, in which the average velocity at the inlet is $U = 1$, the height of the square $H = 1/4$, and the kinematic viscosity $\nu = 0.001$. We compute the flow by using the fourth order method with three resolutions: $h = 1/192$, 1/288 and 1/384. We take the time step as $\Delta t = 0.32h$ in the calculation. It can be verified that the constraint (2.29) is satisfied so that the stability of the whole algorithm is assured.

The stream function and vorticity plots from $t = 0.75$ to 2 are shown in Figs. 5–10, respectively. Many interesting phenomenon, such as formation and disappearance of a bubble, spin off for a shear flow, boundary layer separation, and vortex roll-up, can be observed in the physical process. Such a flow pattern can also be observed by the corresponding physical experiments reported in [21].

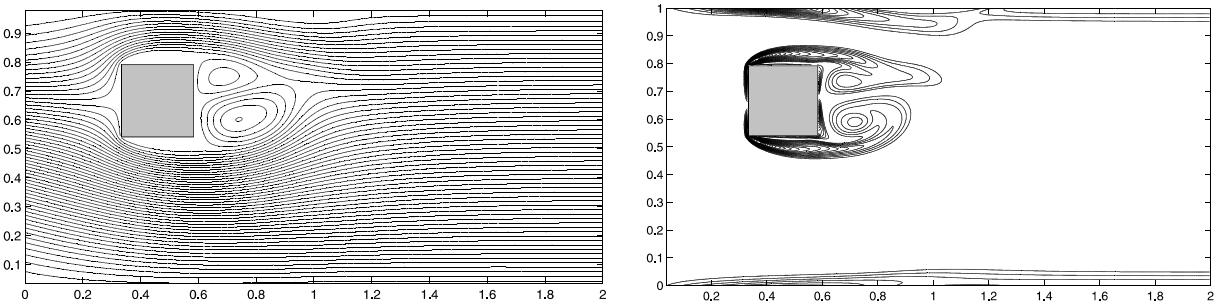

Fig. 5. Stream function and vorticity plots for the flow past a non-symmetric square at $t = 0.75$. The Reynolds number is $Re = 250$. The fourth order method is used, at the resolution 577×289.

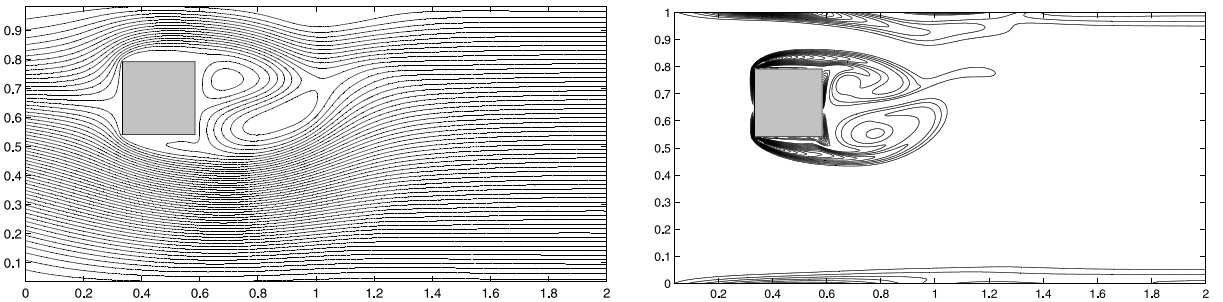

Fig. 6. Stream function and vorticity plots for the flow past a non-symmetric square at $t = 1$, using the same resolution and physical parameters as in Fig. 5.

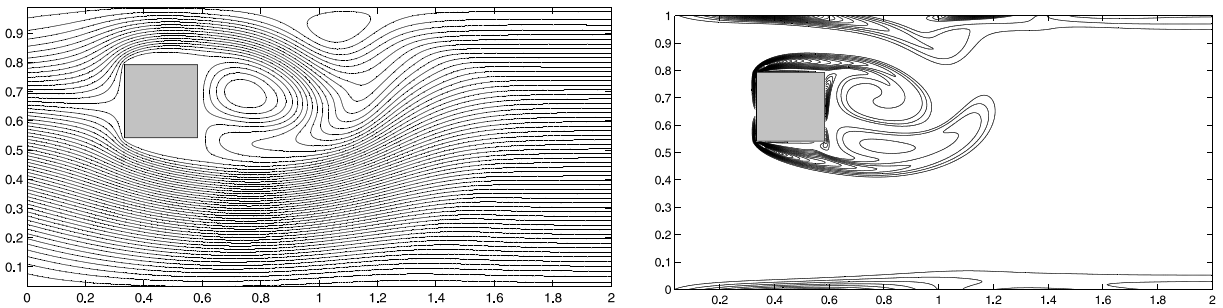

Fig. 7. Stream function and vorticity plots for the flow past a non-symmetric square at $t = 1.25$, using the same resolution and physical parameters as in Fig. 5.

To illustrate the unsteady nature of the flow, we record the time history of the boundary value of the stream function on the cylinder square, along with the vertical velocity component v at a sample point $P^* = (2/3, 2/3)$. The results are presented in Fig. 11, which also shows the non-symmetric feature of the flow due to the non-zero profile of v. It is indicated that the flow becomes more and more non-symmetric as time goes on.

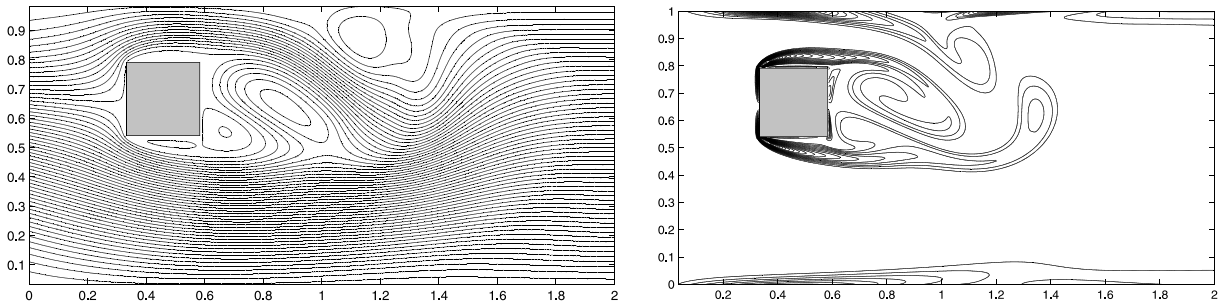

Fig. 8. Stream function and vorticity plots for the flow past a non-symmetric square at $t = 1.5$, using the same resolution and physical parameters as in Fig. 5.

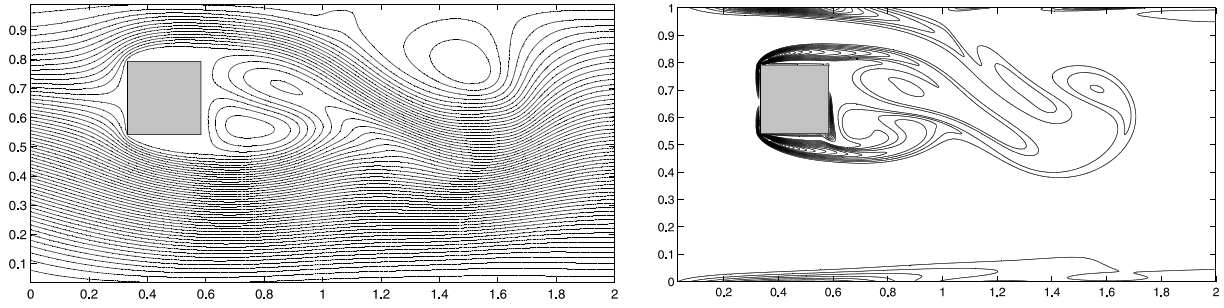

Fig. 9. Stream function and vorticity plots for the flow past a non-symmetric square at $t = 1.75$, using the same resolution and physical parameters as in Fig. 5.

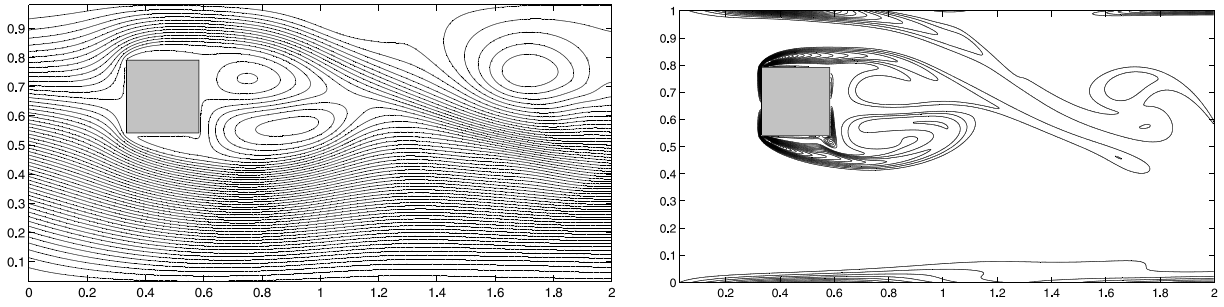

Fig. 10. Stream function and vorticity plots for the flow past a non-symmetric square at $t = 2$, using the same resolution and physical parameters as in Fig. 5.

The vorticity profiles calculated by using the three resolutions are compared at the cut $x = 0.75$ when $t = 1$. The plot is shown in Fig. 12, in which a good agreement can be seen.

In addition, the stream function values at $t = 1$, computed by using the three resolutions, are reported in Tables 7 and 8 at the following six points:

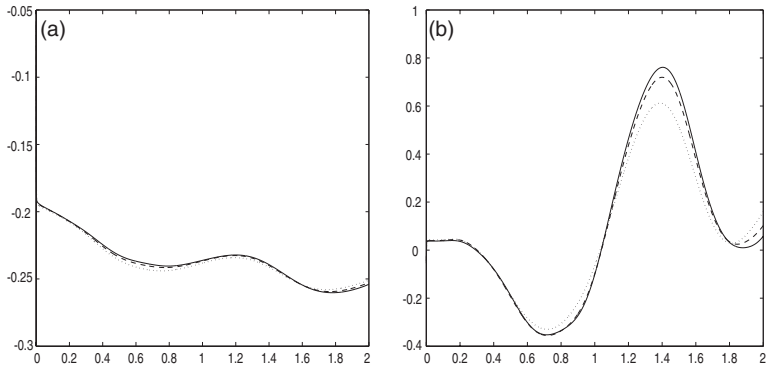

Fig. 11. (a) Time evolution of the value of the stream function on the square cylinder boundary. (b) Time evolution of the vertical velocity at a sample point $P^* = (2/3, 2/3)$. The solid line represents the result computed by the resolution $h = 1/384$, the dashed line represents that of $h = 1/288$, and the dotted line represents that of $h = 1/192$.

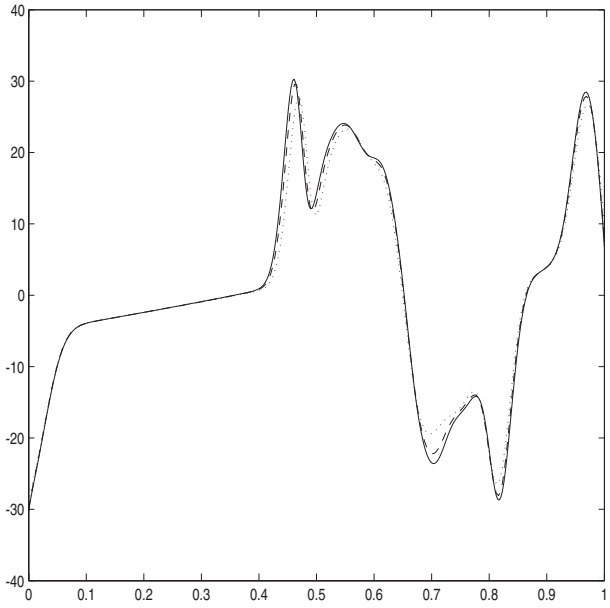

Fig. 12. Comparison of vorticity profile of the flow past a non-symmetric square, at $x = 0.75$ cut for $t = 1$, using three resolutions: $h = 1/192$, 1/288 and 1/384. The solid line represents the result computed by the resolution $h = 1/384$, the dashed line represents that of $h = 1/288$, and the dotted line represents that of $h = 1/192$.

$$P_1 = \left(\frac{1}{2}, \frac{20}{24}\right), \quad P_2 = \left(\frac{2}{3}, \frac{17}{24}\right), \quad P_3 = \left(\frac{3}{4}, \frac{17}{24}\right), \quad P_1' = \left(\frac{1}{2}, \frac{12}{24}\right), \quad P_2' = \left(\frac{2}{3}, \frac{15}{24}\right),$$
$$P_3' = \left(\frac{3}{4}, \frac{15}{24}\right). \tag{4.9}$$

Table 7
Values of the stream function for the flow past a non-symmetric square at P_1, P_2, P_3, using three different resolutions

Resolution	Time: $t = 1$, time step size: $\Delta t = 0.32h$		
	$P_1 = (\frac{1}{2}, \frac{5}{6})$	$P_2 = (\frac{2}{3}, \frac{17}{24})$	$P_3 = (\frac{3}{4}, \frac{17}{24})$
385×193	−2.510981e−01	−2.053396e−01	−2.161120e−01
577×289	−2.437447e−01	−2.037708e−01	−2.137329e−01
769×385	−2.410204e−01	−2.028040e−01	−2.116595e−01

Table 8
Values of the stream function for the flow past a non-symmetric square at P_1', P_2', P_3', using three different resolutions

Resolution	Time: $t = 1$, time step size: $\Delta t = 0.32h$		
	$P_1' = (\frac{1}{2}, \frac{1}{2})$	$P_2' = (\frac{2}{3}, \frac{5}{8})$	$P_3' = (\frac{3}{4}, \frac{5}{8})$
385×193	−2.401009e−01	−2.551152e−01	−2.896303e−01
577×289	−2.423052e−01	−2.581289e−01	−2.947009e−01
769×385	−2.428560e−01	−2.594935e−01	−2.961160e−01

Note that P_i' is symmetric to P_i, $i = 1, 2, 3$, with respect to $y = 16/24$. Obviously the two tables provide additional numerical evidence of the non-symmetric feature of the flow.

4.3. Flow past a heat exchanger

In this sub-section we present numerical simulation for an impulsively started incompressible flow in the following region (see Fig. 13), as a further evidence of accuracy and efficiency of our method.

The flow region is similar to that of a heat exchanger, which is used to model an idealized 2-D cross section to study the cooling patterns set up by air currents. In this article, the detailed dimensions are given by: $OO_1 = OT = 1$, $OR = O_1R_1 = 1/8$. The inlet points B and M have coordinates (w.r.t. the origin O) (0, 1/4), (0, 3/8), respectively. The coordinates of the other corner points are

$$A\left(0, \frac{1}{8}\right), \quad C\left(\frac{3}{16}, \frac{1}{4}\right), \quad D\left(\frac{3}{16}, \frac{3}{4}\right), \quad E\left(\frac{9}{32}, \frac{3}{4}\right), \quad F\left(\frac{9}{32}, \frac{1}{8}\right). \tag{4.10}$$

The positions of the outlet points are also determined by their coordinates

$$P\left(\frac{3}{16}, 0\right), \quad Q\left(\frac{3}{16}, -\frac{1}{8}\right), \quad R\left(0, -\frac{1}{8}\right). \tag{4.11}$$

In addition, there are three boxes in the middle, which are denoted by $S_1S_2U_2U_1$, $S_3S_4U_4U_3$, and $S_5S_6U_6U_5$. The x-coordinates of S_1, S_2, S_3, S_4, S_5 and S_6 are given by 11/32, 13/32, 15/32, 17/32, 19/32 and 21/32, and the y-coordinates of U_1 and S_1 are given by 3/8 and 3/4, respectively. The coordinates of A_1–T_1 can be obtained by symmetry.

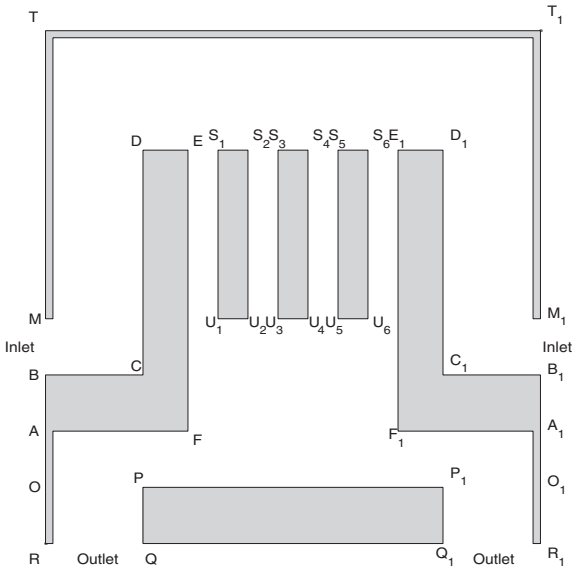

Fig. 13. A multi-connected domain of a heat exchanger.

The no-penetration, no-slip boundary condition $\boldsymbol{u}|_{\Gamma} = 0$ is imposed on the boundaries of the region, except for the inlet BM, B_1M_1, and outlet QR, Q_1R_1. At the inlet BM, the velocity field is given by the standard parabolic profile

$$u = 384\left(\frac{3}{8} - y\right)\left(y - \frac{1}{4}\right), \quad v = 0, \tag{4.12}$$

and consequently, the velocity profile at the inlet B_1M_1 is

$$u = -384\left(\frac{3}{8} - y\right)\left(y - \frac{1}{4}\right), \quad v = 0. \tag{4.13}$$

Similarly, integrating the velocity field gives the boundary condition for ψ at the inlet:

$$\text{On } BM, \quad \psi_{\mathrm{b}} = -1.5\left(y - \frac{1}{4}\right) + 128\left(y - \frac{5}{16}\right)^3 + \frac{3}{32}, \tag{4.14}$$

and

$$\text{On } B_1M_1, \quad \psi_{\mathrm{b}} = 1.5\left(y - \frac{1}{4}\right) - 128\left(y - \frac{5}{16}\right)^3 - \frac{3}{32}. \tag{4.15}$$

The other boundary values for ψ are given by

$$\begin{aligned}
&\text{On } RA, AF, FE, ED, DC, CB, BA, \quad \psi_{\mathrm{b}} = \tfrac{1}{8},\\
&\text{On } R_1A_1, A_1F_1, F_1E_1, E_1D_1, D_1C_1, C_1B_1, B_1A_1, \quad \psi_{\mathrm{b}} = -\tfrac{1}{8},\\
&\text{On } MT, TT_1, T_1M_1, \quad \psi_{\mathrm{b}} = 0,\\
&\text{On } QP, PP_1, P_1Q_1, \quad \psi_{\mathrm{b}} = 0.
\end{aligned} \tag{4.16}$$

Again, we use the natural normal boundary conditions at the outlet

$$\text{On } RQ, R_1Q_1, \qquad \frac{\partial \psi}{\partial \boldsymbol{n}} = 0, \quad \frac{\partial \boldsymbol{u}}{\partial \boldsymbol{n}} = 0, \quad \frac{\partial \omega}{\partial \boldsymbol{n}} = 0. \tag{4.17}$$

The boundary value for ψ on the middle box $\Gamma_2 = S_3S_4U_4U_3$ can be obtained by symmetry

$$\psi_b = 0, \quad \text{on } \Gamma_2. \tag{4.18}$$

The boundary condition for ψ at the other two cooling boxes: $\Gamma_1 = S_1S_2U_2U_1$, $\Gamma_3 = S_5S_6U_6U_5$ cannot be obtained directly. The fixed point iterative process described earlier has to be carried out to get these constants.

A numerical simulation of the flow with a similar geometry was provided in an earlier literature [12]. Such a calculation is based on the general vortex method package described in [27]. Nevertheless, only a rough and brief structure of the flow can be observed by using the vortex method. See Fig. 3.6 in [12]. To analyze a detailed structure of the the streamline and vorticity, we use the fourth order method proposed in Section 3 to compute the flow. The Reynolds number is taken as $Re = (UL)/v = 2000$, with the average velocity at the inlet $U = 1$, the engine length $L = 1$, and $v = 0.0005$. The calculations were carried out by using three grid sizes: $\Delta x = \Delta y = 1/512$, $\Delta x = \Delta y = 1/768$ and $\Delta x = \Delta y = 1/1024$, respectively. Regarding the time step, we take $\Delta t = 0.32h$, which can be verified to satisfy (2.29), so that the overall scheme is stable. The vorticity profiles computed by using the grid $\Delta x = \Delta y = 1/512$ at a sequence of times, i.e., $t_1 = 0.5$,

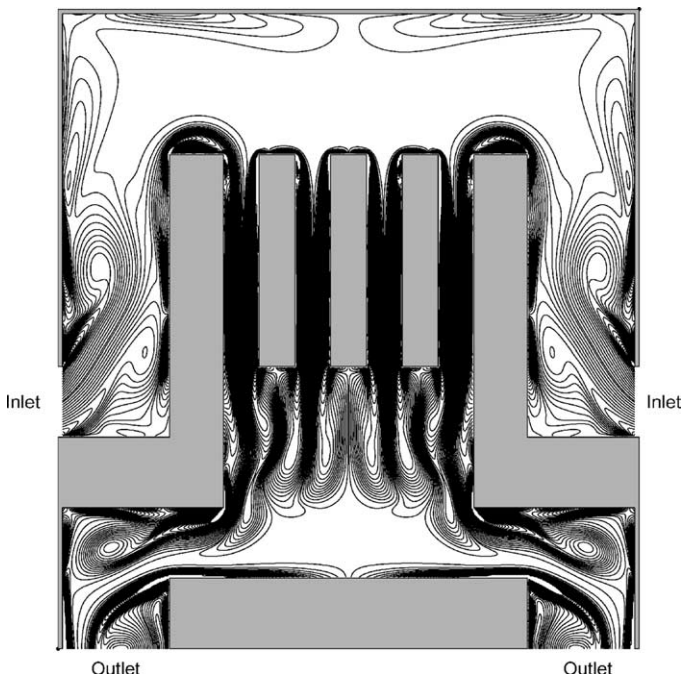

Fig. 14. Vorticity plots at $t_1 = 0.5$ for the flow past the heat exchanger at Reynolds number $Re = 2000$. The computation is based on the fourth order method, at the resolution $h = 1/512$. Thirty equally spaced contours from 1 to 100 and from −100 to −1, 20 equally spaced contours from 100 to 1000 and from −1000 to −100, are shown.

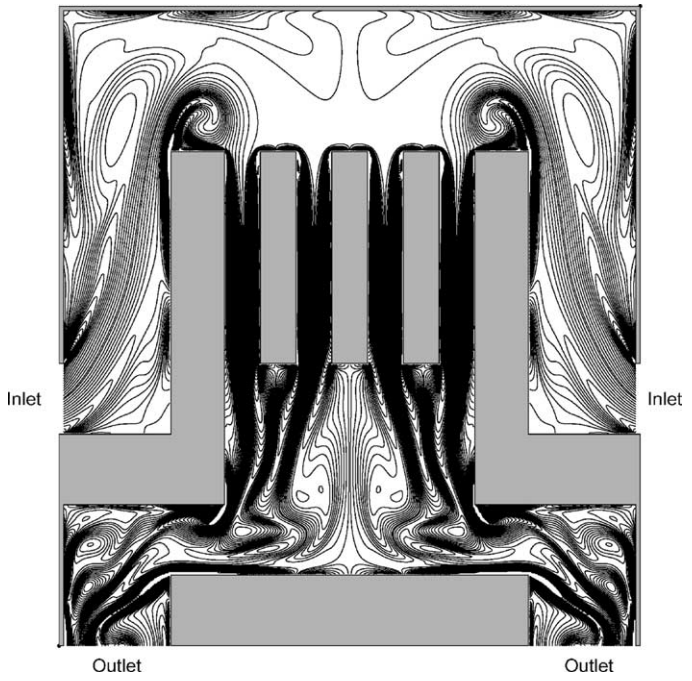

Fig. 15. Vorticity plot at $t_2 = 1$, using the same resolution and the same contour levels as in Fig. 14.

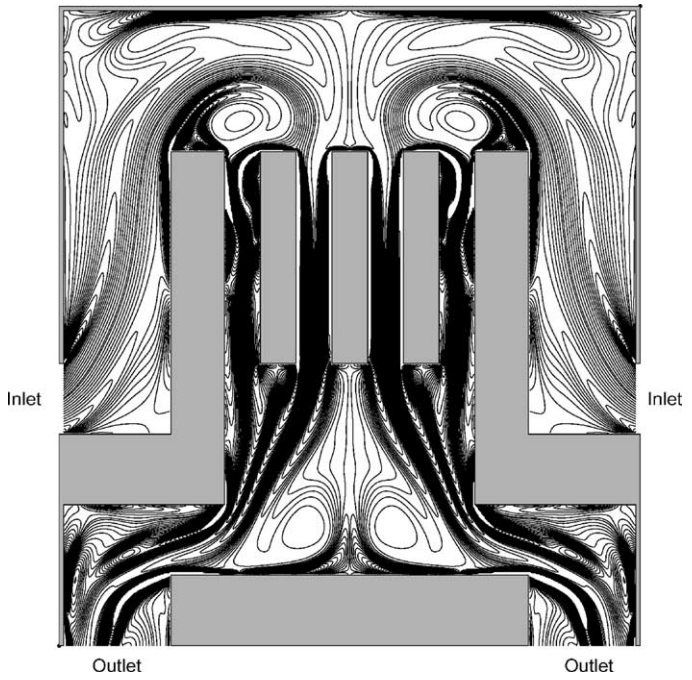

Fig. 16. Vorticity plot at $t_3 = 1.5$, using the same resolution and the same contour levels as in Fig. 14.

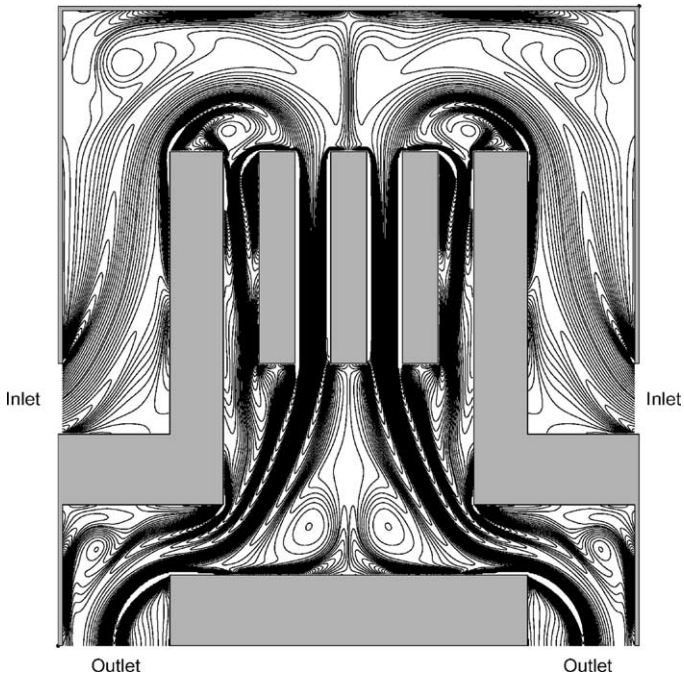

Fig. 17. Vorticity plot at $t_4 = 2$, using the same resolution and the same contour levels as in Fig. 14.

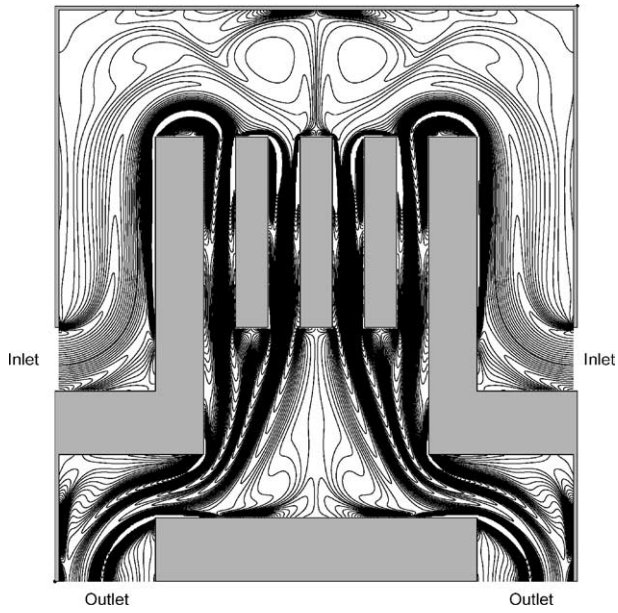

Fig. 18. Vorticity plot at $t = 6$, using the same resolution and the same contour levels as in Fig. 14.

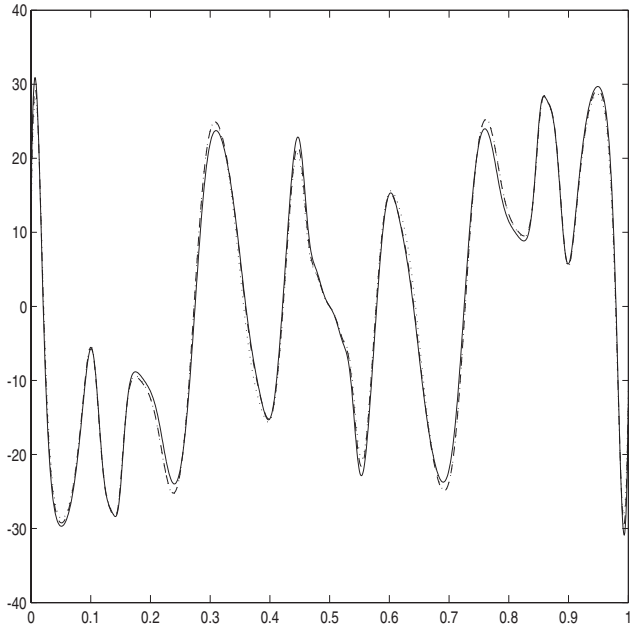

Fig. 19. Comparison of vorticity profile of the flow past a heat exchanger, at $y = 1/16$ cut for $t = 1$, using three resolutions: $h = 1/512$, 1/768 and 1/1024. The solid line represents the result computed by the resolution $h = 1/1024$, the dashed line represents that of $h = 1/768$, and the dotted line represents that of $h = 1/512$.

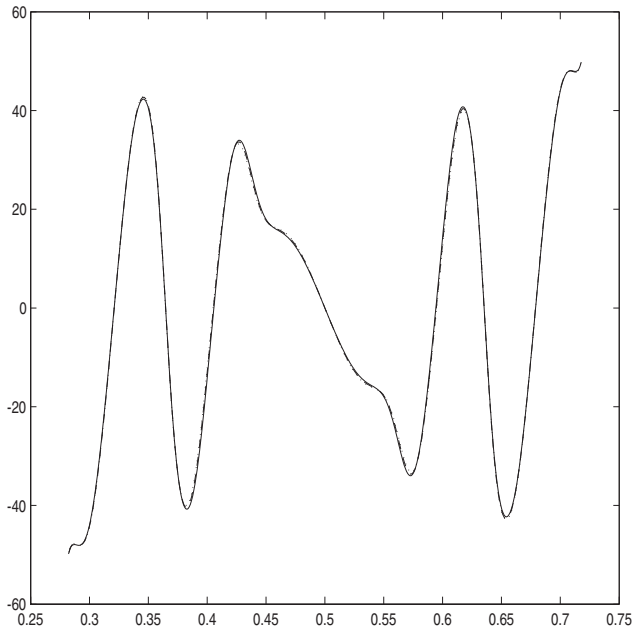

Fig. 20. Comparison of the vorticity profile of the flow past a heat exchanger, at $y = 1/4$ cut for $t = 1$, using three resolutions: $h = 1/512$, 1/768 and 1/1024.

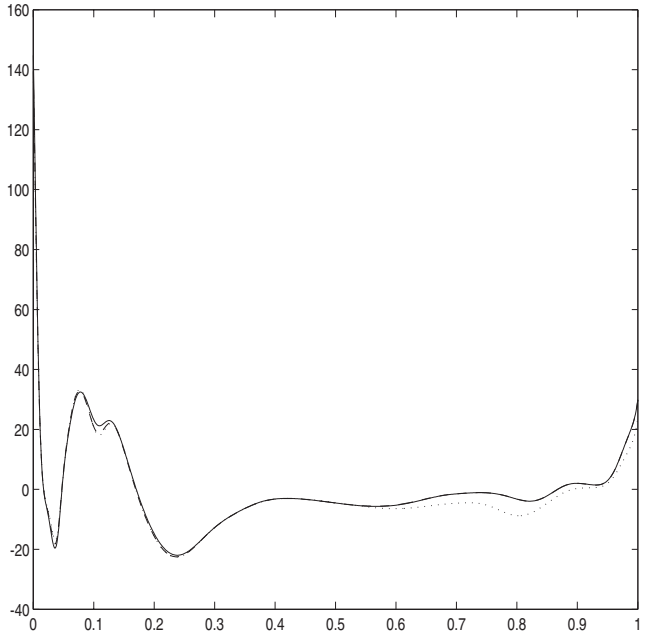

Fig. 21. Comparison of the vorticity profile of the flow past a heat exchanger, at $x = 5/16$ cut for $t = 1$, using three resolutions: $h = 1/512$, 1/768 and 1/1024.

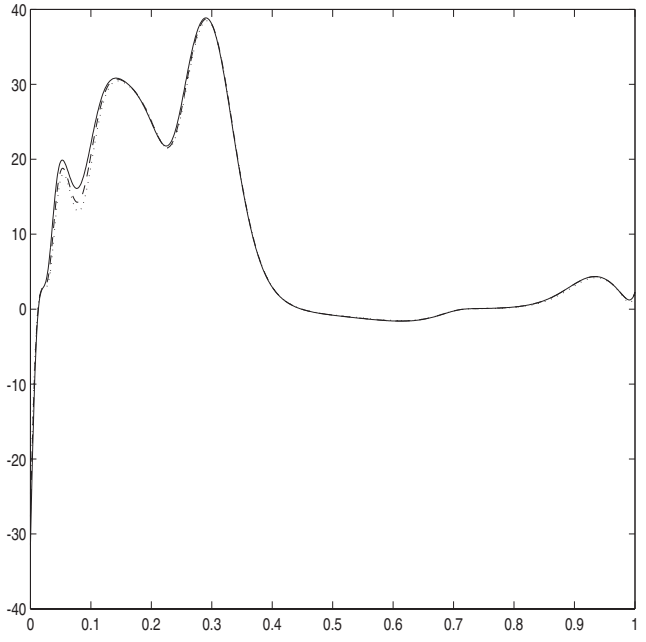

Fig. 22. Comparison of the vorticity profile of the flow past a heat exchanger, at $x = 7/16$ cut for $t = 1$, using three resolutions: $h = 1/512$, 1/768 and 1/1024.

$t_2 = 1$, $t_3 = 1.5$, $t_4 = 2$ are shown in Figs. 14–17, respectively. Fig. 18 shows the vorticity profile at a later time, $t = 6$.

For accuracy verification, the vorticity profiles computed by the three resolutions are compared at time $t = 1$ on $y = 1/16$, $y = 1/4$, $x = 5/16$, $x = 7/16$, in Figs. 19–22, respectively. It can be seen that the results using the three resolutions match very well.

5. Conclusion remarks

In this paper, both the second and fourth order finite difference methods are developed for the 2-D incompressible flow in a multi-connected domain based on the vorticity–stream function formulation. The key point is the discrete realization of boundary condition (1.5d), which results in an iterative formula to determine the stream function constant values on the boundary sections of the "holes". The robustness of the proposed methods are shown by the numerical experiments.

Acknowledgement

This research was supported by NSF grant DMS-0107218.

Appendix A. Proof of proposition 3.1

Proof. Using the notation of Section 2, we denote by $\widetilde{\psi} = \psi^1 - \psi^2$, where ψ^1, ψ^2 are the solutions of (3.8) with boundary conditions $\psi^1|_{\Gamma_1} = C_1$, $\psi^2|_{\Gamma_1} = C^2$, respectively. Then

$$\begin{cases} \left(\Delta_h + \frac{h^2}{6} \mathrm{D}_x^2 \mathrm{D}_y^2\right) \widetilde{\psi} = 0, \\ \widetilde{\psi}|_{\Gamma_0} = 0, \quad \widetilde{\psi}|_{\Gamma_1} = C_1 - C_2. \end{cases} \tag{A.1}$$

The definition of ϕ in (3.9) indicates that

$$\phi(C_1) - \phi(C_2) = \frac{1}{|\Gamma_1|} \left(\frac{3}{2} \int_{\Gamma_1}^{(1)} \widetilde{\psi} - \frac{3}{5} \int_{\Gamma_1}^{(2)} \widetilde{\psi} + \frac{1}{10} \int_{\Gamma_1}^{(3)} \widetilde{\psi} \right). \tag{A.2}$$

As can be seen, the right-hand side of (A.2) is different from (2.12) in the second order case: three integrals, $\int_{\Gamma_1}^{(1)} \widetilde{\psi}$, $\int_{\Gamma_1}^{(2)} \widetilde{\psi}$, $\int_{\Gamma_1}^{(3)} \widetilde{\psi}$ are involved in (A.2), whereas only $\int_{\Gamma_1}^{(1)} \widetilde{\psi}$ was involved in (2.12). A better estimate of (A.2) can be obtained by rewriting it. Motivated by the idea of the stability analysis of the vorticity boundary conditions, which were shown in [8], we can write $(3/2)\widetilde{\psi}_{n-1,j} - (3/5)\widetilde{\psi}_{n-2,j} + (1/10)\widetilde{\psi}_{n-3,j}$ as

$$\frac{3}{2}\widetilde{\psi}_{n-1,j} - \frac{3}{5}\widetilde{\psi}_{n-2,j} + \frac{1}{10}\widetilde{\psi}_{n-3,j} = \frac{2}{5}\widetilde{\psi}_{n,j} + \frac{3}{5}\widetilde{\psi}_{n-1,j} - \frac{2}{5}h^2 \mathrm{D}_x^2 \widetilde{\psi}_{n-1,j} + \frac{1}{10}h^2 \mathrm{D}_x^2 \widetilde{\psi}_{n-2,j}. \tag{A.3}$$

The substitution of (A.3) into (A.2), along with the fact that $\widetilde{\psi}$ is a constant $C_1 - C_2$ on Γ_1, gives

$$\phi(C_1) - \phi(C_2) = \frac{1}{|\Gamma_1|}\left(\frac{2}{5}(C_1 - C_2)|\Gamma_1| + \frac{3}{5}\int_{\Gamma_1}^{(1)} \widetilde{\psi} - \frac{2}{5}h^2 \int_{\Gamma_1}^{(2)} D_{\boldsymbol{n}}^2\widetilde{\psi} + \frac{1}{10}h^2 \int_{\Gamma_1}^{(3)} D_{\boldsymbol{n}}^2\widetilde{\psi}\right), \tag{A.4}$$

where $D_{\boldsymbol{n}}^2\widetilde{\psi}$ is $\mathrm{D}_x^2\widetilde{\psi}$ on the boundary sections AB, CD, and $\mathrm{D}_y^2\widetilde{\psi}$ on the boundary sections BC, DA.

The following lemma, which is analogous to Lemma 2.2 in the second order case, gives the estimate of $\widetilde{\psi}$ near the boundary Γ_1. The strategy of the proof is also similar to that of Lemma 2.2 and involves an application of the maximum principle to the operator $(\Delta_h + (h^2/6)\mathrm{D}_x^2\mathrm{D}_y^2)$.

Lemma A.1. *Let u be the solution of the system*

$$\begin{cases} \left(\Delta_h + \frac{h^2}{6}\mathrm{D}_x^2\mathrm{D}_y^2\right)u = 0, \\ u|_{\Gamma_0} = 0, \quad u|_{\Gamma_1} = 1. \end{cases} \tag{A.5}$$

Then we have

$$0 \leqslant u_{n-k,j} \leqslant 1 - kh \quad \text{for } n \leqslant j \leqslant m. \tag{A.6}$$

Proof. With the same notation as in the proof of Lemma 2.2, the region Ω can be partitioned into four sub-regions: A_1ABB_1, A_1ADD_1, D_1DCC_1, C_1CBB_1, denoted by Ω_1, Ω_2, Ω_3, Ω_4, respectively, as shown in Fig. 3. The same function v as in (2.15) is considered. Detailed calculations indicate that the function v constructed in (2.15) is concave, and satisfies

$$\begin{cases} \left(\Delta_h + \frac{h^2}{6}\mathrm{D}_x^2\mathrm{D}_y^2\right)v \leqslant 0, \\ v|_{\Gamma_0} = 0, \quad v|_{\Gamma_1} = 1. \end{cases} \tag{A.7}$$

Then, clearly, $f = -(\Delta_h + (h^2/6)\mathrm{D}_x^2\mathrm{D}_y^2)v \geqslant 0$. Also, u can be decomposed into two parts: $u = v + w$, where w is the solution of the following system

$$\begin{cases} \left(\Delta_h + \frac{h^2}{6}\mathrm{D}_x^2\mathrm{D}_y^2\right)w = f \geqslant 0, \\ w|_{\Gamma_0} = 0, \quad w|_{\Gamma_1} = 0. \end{cases} \tag{A.8}$$

It can be argued, as in Section 2, that the maximum principle holds for the operator $(\Delta_h + (h^2/6)\mathrm{D}_x^2\mathrm{D}_y^2)$. In a uniform grid, the operator has the form

$$\left(\Delta_h + \frac{h^2}{6}\mathrm{D}_x^2\mathrm{D}_y^2\right)u_{i,j} = \frac{1}{6h^4}\left((u_{i-1,j-1} + 4u_{i,j-1} + u_{i+1,j-1}) + (4u_{i-1,j} - 20u_{i,j} + 4u_{i+1,j}) + (u_{i-1,j+1} + 4u_{i,j+1} + u_{i+1,j+1})\right), \tag{A.9}$$

so that the maximum principle is valid. This principle together with (A.8) shows that $w \leqslant 0$ at all grid points. Then we have

$$u \leqslant v \quad \text{at all grid points}, \tag{A.10}$$

and in particular, $u_{n-k,j} \leqslant v_{n-k,j} = 1 - kh$. The first part of (A.6) comes directly from the maximum principle of the operator $(\Delta_h + (h^2/6)\mathrm{D}_x^2\mathrm{D}_y^2)$. Lemma A.1 is thus proven. □

Obviously, $\widetilde{\psi} = (C_1 - C_2)u$, where $\widetilde{\psi}$ was given in Eq. (A.1) and u is the solution of (A.5), which results in a bound of the second term in (A.4):

$$\frac{3}{5}\left|\int_{\Gamma_1}^{(1)} \widetilde{\psi}\right| \leqslant \frac{3}{5}(1-h)|C_1 - C_2||\Gamma_1|. \tag{A.11}$$

The estimates of the last two terms in (A.4) are obtained by the following lemma.

Lemma A.2. *Let u be the solution of* (A.5). *Then we have*

$$h^2\left|\int_{\Gamma_1}^{(1)} D_{\boldsymbol{n}}^2 u\right|, \quad h^2\left|\int_{\Gamma_1}^{(2)} D_{\boldsymbol{n}}^2 u\right| \leqslant 4h. \tag{A.12}$$

Proof. For simplicity, only the integral on the boundary section AB is discussed here. The boundary sections BC, CD, DA can be dealt with in the same way. The equation in (A.5) gives $\mathrm{D}_x^2 u = -\left(\mathrm{D}_y^2 + (h^2/6)\mathrm{D}_x^2\mathrm{D}_y^2\right)u$, and its application to the grid point $(n-1, j)$ results in

$$\mathrm{D}_x^2 u_{n-1,j} = -\left(\mathrm{D}_y^2 + \frac{h^2}{6}\mathrm{D}_x^2\mathrm{D}_y^2\right)u_{n-1,j} = -\frac{1}{6}\mathrm{D}_y^2 u_{n-2,j} - \frac{2}{3}\mathrm{D}_y^2 u_{n-1,j} - \frac{1}{6}\mathrm{D}_y^2 u_{n,j}. \tag{A.13}$$

Integration of (A.13) along the boundary AB (by the trapezoidal rule) gives

$$\begin{aligned} h^2\int_{AB}\mathrm{D}_x^2 u_{n-1,j} = &-\frac{1}{6}h^2\left(\frac{1}{2}\frac{u_{n-2,m+1}-u_{n-2,m-1}}{h} - \frac{1}{2}\frac{u_{n-2,n+1}-u_{n-2,n-1}}{h}\right) \\ &-\frac{2}{3}h^2\left(\frac{1}{2}\frac{u_{n-1,m+1}-u_{n-1,m-1}}{h} - \frac{1}{2}\frac{u_{n-1,n+1}-u_{n-1,n-1}}{h}\right) \\ &-\frac{1}{6}h^2\left(\frac{1}{2}\frac{u_{n,m+1}-u_{n,m-1}}{h} - \frac{1}{2}\frac{u_{n,n+1}-u_{n,n-1}}{h}\right). \end{aligned} \tag{A.14}$$

As argued earlier, the application of the maximum principle in (A.5) shows that

$$0 \leqslant u_{i,j} \leqslant 1 \quad \text{for } (x_i, y_j) \in \Omega. \tag{A.15}$$

The combination of (A.14) and (A.15) gives

$$h^2\left|\int_{AB}\mathrm{D}_x^2 u_{n-1,j}\right| \leqslant h. \tag{A.16}$$

Similar estimates can be applied to boundary sections BC, CD, DA. Lemma A.2 is thus proven. □

As mentioned earlier, $\widetilde{\psi} = (C_1 - C_2)u$. The combination of (A.4), Lemmas A.1 and A.2, gives

$$\begin{aligned} |\phi(C_1) - \phi(C_2)| &\leqslant \frac{1}{|\Gamma_1|}\left(\frac{2}{5}|\Gamma_1||C_1 - C_2| + \frac{3}{5}|\Gamma_1||C_1 - C_2|(1-h) + \frac{8}{5}h|C_1 - C_2| + \frac{2}{5}h|C_1 - C_2|\right) \\ &= \left(1 - \frac{3}{5}h + \frac{2}{|\Gamma_1|}h\right)|C_1 - C_2| = \left(1 - \frac{1}{10}h\right)|C_1 - C_2|, \end{aligned} \tag{A.17}$$

since $|\Gamma_1| = 4$. Proposition 3.1 is proven. □

References

[1] Anderson C, Reider M. A high order explicit method for the computation of flow about a circular cylinder. J Comput Phys 1996;21:207–24.
[2] Bade H, Dennis S, Young P. Steady and unsteady flow past a rotating circular cylinder at low Reynolds numbers. Comput Fluids 1989;17:579–609.
[3] Briley W. A numerical study of laminar separation bubbles using the Navier–Stokes equations. J Fluid Mech 1971;47:713–36.
[4] Álessio D, Dennis S. A method of domain decomposition for calculating the steady flow past a cylinder. J Eng Math 1994;28:227–40.
[5] Álessio D, Dennis S. A vorticity model for viscous flow past a cylinder. Comput Fluids 1994;23:279–93.
[6] Dennis S, Hudson J. Compact h^4 finite-difference approximations to operators of Navier–Stokes type. J Comput Phys 1989;85:390–416.
[7] Weinan E, Liu L-G. Vorticity boundary condition for finite difference schemes. J Comput Phys 1996;124:368–82.
[8] Weinan E, Liu L-G. Essentially compact schemes for unsteady viscous incompressible flows. J Comput Phys 1996;126:122–38.
[9] Glowinski R, Pironneau O. Numerical methods for the first biharmonic equation and for the two-dimensional Stokes problem. SIAM Rev 1979;21:167–212.
[10] Gresho P. Incompressible fluid dynamics: some fundamental formulation issues. Ann Rev Fluid Mech 1991;23:413–53.
[11] Gunzburger M. Finite element methods for viscous incompressible flows: a guide to theory, practice, and algorithms. Boston: Academic Press; 1989.
[12] Gustafson K, Sethian J. Vortex methods and vortex motion. SIAM; 1991.
[13] Henshaw W, Kreiss H-O, Reyna L. A fourth-order accurate difference approximation for the incompressible Navier–Stokes equations. Comput Fluids 1994;23:575–93.
[14] Hou T, Wetton B. Convergence of a finite difference scheme for the Navier–Stokes equations using vorticity boundary conditions. SIAM J Numer Anal 1992;29:615–39.
[15] Ingham D, Tang T. A numerical investigation into the steady flow past a rotating circular cylinder at low and intermediate Reynolds numbers. J Comput Phys 1990;87:91–107.
[16] Johnston H, Liu J-G. A Finite difference scheme for incompressible flow based on local pressure boundary conditions. J Comput Phys 2002;80:120–54.
[17] Kreiss H-O. Comparison of accurate methods for the integration of hyperbolic equations. Tellus XXIV 1972;3:199–215.
[18] Li M, Tang T, Fornberg B. A compact fourth-order finite difference scheme for the steady incompressible Navier–Stokes equations. Int J Numer Methods Fluids 1995;20:1137.
[19] Liu J-G, Weinan E. Simple finite element method in vorticity formulation for incompressible flow. Math Comput 2001;70:579–93.
[20] Mizukami A. A stream function-vorticity finite element formulation for Navier–Stokes equations in multi-connected domain. Int J Numer Methods Eng 1983;19:1403–9.
[21] Okajima A. Strouhal numbers of rectangular cylinders. J Fluid Mech 1982;123:379–98.
[22] Orszag S, Israeli M. Numerical simulation of viscous incompressible flows. Ann Rev Fluid Mech 1974;6:281–318.
[23] Orszag S, Israeli M, Deville M-O. Boundary conditions for incompressible flows. J Sci Comput 1986;1:75–111.
[24] Peyret R, Taylor T. Computational methods for fluid flow. New York/Berlin: Springer-Verlag; 1983.
[25] Quartapelle L. Vorticity conditioning in the computation of two-dimensional viscous flow. J Comput Phys 1981;40:453–77.
[26] Quartapelle L. Numerical solution of the incompressible Navier–Stokes equations. Berlin: Birkhauser; 1983.
[27] Settles GS. Modern developments in flow visualization. AIAA J 1986;24:1313–23.
[28] Stella F, Guj G. Vorticity–velocity formulation in the computation of flows in multi-connected domains. Int J Numer Methods Fluids 1989;9:1285–98.
[29] Tang T, Ingham D. On steady flow past a rotating circular cylinder at Reynolds numbers 60 and 100. Comput Fluids 1991;19:217–30.

[30] Tezduyar T. Finite element formulation for the vorticity–stream function form of the incompressible Euler equations on multi-connected domains. Comput Methods Appl Mech Eng 1989;73(3):331–40.
[31] Thom A. The flow past circular cylinders at low speeds. Proc R Soc London Sect A 1933;141:651–69.
[32] Wang C, Liu J-G. Analysis of finite difference schemes for unsteady Navier–Stokes equations in vorticity formulation. Numer Math 2002;91(2):543–76.